Band Structures of Transition-Metal-Dichalcogenide Layer Compounds

L. F. Mattheiss
Bell Laboratories, Murray Hill, New Jersey 07974
(Received 6 June 1973)

The nonrelativistic augmented-plane-wave (APW) method is applied to calculate the electronic band structures of several transition-metal-dichalcogenide (TX_2) layer compounds, including materials with the $C6$ ($1T$-HfS_2, $1T$-TaS_2), $C27$ ($2H$-TaS_2, $2H$-$NbSe_2$), and $C7$ ($2H$-MoS_2) structure types. These calculations involve crystal potentials that are derived from neutral-atom charge densities. The results of these calculations confirm that the group-IVB ($1T$-HfS_2) and group-VIB ($2H$-MoS_2) compounds are semiconductors; the calculated indirect band gaps of 2.7 and 1.2 eV are in reasonable agreement with the observed values of 2.0 and 1.4 eV, respectively. Metallic behavior is predicted for the intermediate group-VB compounds $1T$-TaS_2, $2H$-TaS_2, and $2H$-$NbSe_2$. A novel feature of the metal d bands in the $2H$-TX_2 compounds is the occurence of a 1-eV hybridization gap within the d_{z^2} and d_{xy}, $d_{x^2-y^2}$ manifolds. This splits off a pair of hybridized d bands which are half-filled in $2H$-TaS_2 and $2H$-$NbSe_2$ and completely filled in $2H$-MoS_2. As a result of this hybridization gap, the valence or conduction bandwidths in each of these $2H$-TX_2 compounds are reduced to about 1 eV.

I. INTRODUCTION

During the past few years, a widespread interest in the structural, optical, electrical, magnetic, and superconducting properties of the transition-metal-dichalcogenide layer compounds has evolved. These compounds have the formula TX_2, where T is a transition-metal atom from the group IVB, VB, or VIB columns of the Periodic Table and X is one of the chalcogens, sulfur, selenium, or tellurium. The diverse physical properties of this broad class of materials have been reviewed in a recent article by Wilson and Yoffe.[1] In general, the dichalcogenides formed from the groups IVB and VIB transition-metal atoms exhibit semiconducting or insulating properties whereas the group VB compounds tend to be metallic.

Structurally, these compounds can be regarded as strongly bonded two-dimensional X-T-X layers or sandwiches which are loosely coupled to one another by relatively weak Van der Waals-type forces. Within a single X-T-X sandwich, the T and X atoms form two-dimensional hexagonal arrays. Depending on the relative alignment of the two X-atom sheets within a single X-T-X sandwich, two distinct two-dimensional crystal structures are obtained. In one, the metal atoms are octahedrally coordinated by six neighboring X atoms, whereas in the other, the coordination of the metal atoms is trigonal prismatic.

Variations in the stacking sequence and registry of successive X-T-X sandwiches along the hexagonal c axis lead to a large number of crystal structures or polytypes in three dimensions. These are referred to as the $1T$, $2H$, $3R$, $4Ha$, $4Hb$, and $6R$ phases. In this abbreviated notation, the integer indicates the number of X-T-X sandwiches per unit cell along the hexagonal c axis and T, H, and R denote trigonal, hexagonal, and rhombohedral symmetries, respectively. The $1T$ phase contains X-T-X sandwiches in which the metal atoms are octahedrally coordinated, whereas the coordination is trigonal prismatic in the $2H$, $3R$, and $4Ha$ phases. In the $4Hb$ and $6R$ polytypes, the coordination within successive sandwiches alternates between octahedral and trigonal prismatic.

It is not surprising that the physical properties of these layer compounds are dominated by these two-dimensional structural characteristics. For example, it is found that single crystals usually grow in the form of thin platelets, and these are readily cleaved to yield samples that are only a few hundred angstroms thick along the c axis. Electrical and thermal conductivities are found to be significantly lower along the c axis than they are within the basal plane. One can often prepare intercalation compounds of the form A_xTX_2, where A is an atom or molecule which occupies the interstitial sites between neighboring X-T-X sandwiches. The semiconducting group IVB and VIB compounds are found to exhibit metallic conductivity when intercalated with alkali atoms. The metallic group VB compounds can often be intercalated with organic molecules. Depending on their size, these molecules can increase the interlayer separations by as much as 50 Å. Most of these metallic compounds superconduct at low temperatures, even when the layers are separated by these organic spacers.

Several semiempirical band-structure and ligand-field models have been proposed to describe the electronic states in these TX_2 layer compounds. Wilson and Yoffe[1] have proposed schematic energy-band models for several groups of TX_2 compounds. Relying heavily on systematic trends that are observed in the optical data, they

estimate valence and conduction bandwidths and band gaps, and correlate these with the observed electrical and structural properties. In a recent series of papers, Bromley, Murray, and Yoffe[2–6] have applied a semiempirical tight-binding method[3] to calculate the band structures for several groups of compounds, including the octahedrally coordinated $1T$-TX_2 compounds (T = Ti, Zr, Hf; X = S, Se, Te)[4,6] as well as the trigonal-prismatic $2H$-TX_2 group VIB compounds (T = Mo, W; X = S, Se, Te).[2,5] The calculations for the $2H$ compounds were carried out in a two-dimensional approximation, though some estimates of interlayer interactions were made in the case of $2H$-MoS_2. Edmondson[7] has carried through a similar calculation for $2H$-MoS_2 in the two-dimensional limit. On the other hand, Goodenough[8] and Huisman *et al.*[9] have utilized the ligand-field or molecular-orbital approach to derive schematic energy-band models for several of these layer-type compounds.

The purpose of the present investigation is to apply the augmented-plane-wave (APW) method to determine the electronic energy bands for several of the less complicated TX_2 polytypes and to compare these results with the experimental data as well as the earlier semiempirical band models. This study involves four TX_2 compounds with three different crystal structures, including compounds with the $C6$ ($1T$-HfS_2, $1T$-TaS_2), $C27$ ($2H$-TaS_2, $2H$-$NbSe_2$), and $C7$ ($2H$-MoS_2) structure types in the "Strukturbericht" classification. Unlike the earlier calculations,[2–7] the present investigation utilizes no empirical results other than the crystal-structure data. The present APW calculations involve approximate crystal potentials that are derived from neutral-atom charge densities. They include corrections to the muffin-tin potential in the unit cell volume that lies outside the APW spheres. A brief summary of the present APW results for $2H$-$NbSe_2$ and $2H$-MoS_2 has been reported in an earlier publication.[10]

The present paper is divided into six sections. In Sec. II we review the physical properties of the various compounds that are considered in this investigation. The computational details of the present study are described in Sec. III, and the APW results are presented in Sec. IV. The APW results for the metal-atom d bands are analyzed in Sec. V in terms of a tight-binding model. Section VI includes a discussion of these results as well as a comparison with experiment. It also contains some comments on previous band and ligand-field models for these compounds.

II. PHYSICAL PROPERTIES

The $1T$-TX_2 and $2H$-TX_2 layer compounds that are involved in this investigation have the D^3_{3d} ($P\bar{3}m1$) and D^4_{6h} ($P6_3/mmc$) space groups, respectively. Although the D^3_{3d} space group belongs to the trigonal system, the Bravais lattice is hexagonal for both space groups. Following Slater,[11] we choose the primitive vectors that generate the hexagonal lattice as

$$\vec{t}_1 = \tfrac{1}{2}a\,(\sqrt{3}\,\hat{i} - \hat{j}),\quad \vec{t}_2 = a\hat{j},\quad \vec{t}_3 = c\hat{k}\,, \tag{1}$$

so that an arbitrary vector $\vec{r}$ can be written in the form $\vec{r} = \xi\vec{t}_1 + \eta\vec{t}_2 + \zeta\vec{t}_3$. Using this coordinate system, we list in Table I the position coordinates of the T and X atoms in the corresponding unit cells for the $C6$, $C27$, and $C7$ crystal structures. The symmetric primitive unit cells are illustrated in Fig. 1. These are drawn approximately to scale, using the observed values for the lattice parameters that are listed in Table II. It is noted that crystal-structure refinements have been carried out only in a few cases so that precise values for the positional parameter z are generally unavailable.

TABLE I. Atom positions in the $1T$-TX_2 and $2H$-TX_2 layer compounds.

$C6$ structure type (D^3_{3d}); $1T$-HfS_2
$(\xi,\ \eta,\ \zeta)_{Hf} = (0,\ 0,\ 0)$
$(\xi,\ \eta,\ \zeta)_S = \pm(\frac{1}{3},\ \frac{2}{3},\ z)$, $z \sim \frac{1}{4}$.
$C27$ structure type (D^4_{6h}); $2H$-TaS_2
$(\xi,\ \eta,\ \zeta)_{Ta} = \pm(0,\ 0,\ \frac{1}{4})$
$(\xi,\ \eta,\ \zeta)_S = \pm(\frac{1}{3},\ \frac{2}{3},\ z)$
$\pm(\frac{1}{3},\ \frac{2}{3},\ \frac{1}{2} - z)$, $z \sim \frac{1}{8}$
$C7$ structure type (D^4_{6h}); $2H$-MoS_2
$(\xi,\ \eta,\ \zeta)_{Mo} = \pm(\frac{1}{3},\ \frac{2}{3},\ \frac{1}{4})$
$(\xi,\ \eta,\ \zeta)_S = \pm(\frac{1}{3},\ \frac{2}{3},\ z - 1)$
$\pm(\frac{1}{3},\ \frac{2}{3},\ \frac{1}{2} - z)$, $z \sim \frac{5}{8}$

It is emphasized that these crystal structures represent the high-temperature phases, particularly in the case of the metallic group-VB compounds. Recent data that are summarized below indicate the occurrence of low-temperature phase transitions in most of the metallic group-VB compounds. Furthermore, large variations are often found to exist in the results of independent lattice-parameter determinations for the same compound. These are due, presumably, either to deviations from perfect stoichiometry or to the coexistence of several phases in at least some samples.

A. $1T$-HfS_2

Based on a simple ionic model, it is reasonable to anticipate that the TX_2 compounds involving the group-IVB transition-metal atoms would be semiconductors or insulators in which the fundamental band gap separates the filled X-atom p bands and the empty T-atom d-band states. Among the group-IVB compounds, $1T$-HfS_2 is an example of

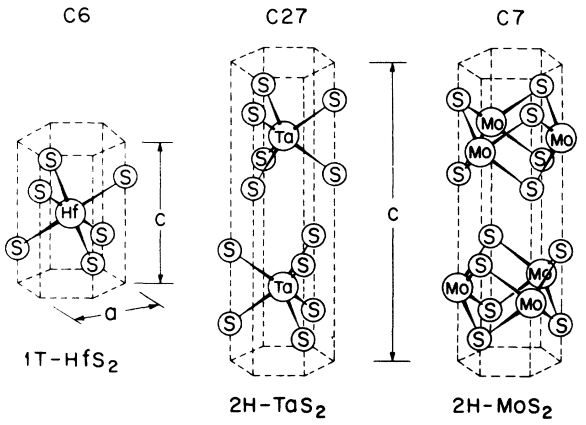

FIG. 1. Symmetric unit cells for the $C6$ ($1T$-HfS_2), $C27$ ($2H$-TaS_2), and $C7$ ($2H$-MoS_2) crystal structures.

one such material that can be prepared with sufficient stoichiometry to allow an electrical determination of the intrinsic gap. From the temperature dependence of the resistivity, Conroy and Park[12] infer a 2.1-eV gap for $1T$-HfS_2 that is in good agreement with the 1.95-eV indirect optical gap that is reported by Greenaway and Nitsche.[13] The latter also observe structure in the reflectivity between 3 and 10 eV. Similar structure has also been observed in transmission spectra[1,14] below 6 eV.

B. $1T$-TaS_2

If this band model is extended to the group-VB compounds, then it predicts that metallic behavior will result from the added electron that now partially fills the T-atom d bands. It is found that the $1T$-TaS_2 polytype is stable only at temperatures above 1050 °K. However, this phase can be maintained at lower temperatures by quenching. Resistivity measurements[15] show that $1T$-TaS_2 is metallic above 350 °K. They reveal that a metal-insulator transition occurs at about 350 °K and that a second transition, involving two semiconducting phases, takes place near 190 °K. Anomalies in the magnetic susceptibility are also reported[16] at these temperatures. Estimates of the activation energy below the metal-insulator transition range from 0.02[15] to 0.1 eV.[17] Recent photoemission studies[18] indicate that the occupied portion of the tantalum 5d conduction band is about 1.5 eV wide and the sulfur 3p valence bandwidth is 6–7 eV.

Wilson and Yoffe[1] were the first to suggest semiconducting behavior for $1T$-TaS_2 at room temperature. They observed that the optical transmission tends to rise rather than fall off at photon energies below 1 eV. Recent room-temperature electron-diffraction studies[19] reveal the presence of a superlattice in $1T$-TaS_2. It is believed[15] that the early reports[1,20] of superconductivity in $1T$-TaS_2 below 0.8 °K are due to mixed-phase ($1T$ and $2H$) samples.

C. $2H$-TaS_2

In contrast to the $1T$ phase, $2H$-TaS_2 remains metallic at low temperatures and becomes superconducting below 0.8 °K. Heat-capacity measurements[21] below 10 °K yield an electronic contribution $\gamma = 8.5$ mJ/mole °K^2. When organic molecules such as pyridine (py) are introduced between the S-Ta-S sandwiches to form the intercalation compound $2H$-TaS_2 $(py)_{1/2}$, the system remains metallic and the superconducting transition temperature is raised to 3.5 °K. The heat capacity γ's for the intercalated compounds are found to increase by 5-10%.[21] Thompson *et al.*[22] have measured the resistivity, magnetic susceptibility, and Hall effect in $2H$-TaS_2. They observe anomalies in these properties at about 70 °K, and these are attributed to a phase transition.

D. $2H$-$NbSe_2$

Evidence for low-temperature phase transitions have also been observed in $2H$-$NbSe_2$. Lee *et al.*[23] have observed a peak in the susceptibility and a sign reversal in the Hall coefficient near $T \approx 40$ °K which they attribute to antiferromagnetic ordering. Subsequent nuclear-magnetic-resonance (NMR) studies by Ehrenfreund *et al.*[24] rule out the existence of magnetic ordering below 40 °K but suggest rather that a change in crystal structure has occurred, since they find evidence for the existence of two inequivalent niobium sites below 40 °K. The results of x-ray studies by Marezio *et al.*[25] at 15 °K are consistent with the room-temperature structure. However, they are also compatible with a distorted structure that involves a slight displacement of the niobium atoms, and this distorted

TABLE II. Structure parameters for TX_2 layer compounds.

Type	TX_2	a (Å)	c (Å)	z
$1T$	HfS_2	3.635[a]	5.837[a]	•••
	TaS_2	3.365[b]	5.853[b]	•••
$2H$	TaS_2	3.316[b]	12.070[b]	•••
	$NbSe_2$	3.440[c]	12.482[c]	0.1163[c]
$2H$	MoS_2	3.160[d]	12.294[d]	0.621[e]

[a]F. K. McTaggart and A. B. Wadsley, Aust. J. Chem. 11, 445 (1958).
[b]Reference 17.
[c]Reference 25.
[d]J. C. Wilderwanck and F. Jellinek, Z. Anorg. Allgem. Chem. 328, 309 (1964).
[e]Reference 29.

structure is consistent with the NMR results.

Superconductivity is observed below 7.0 °K in $2H$-$NbSe_2$, and heat-capacity measurements[26] yield $\gamma = 20.5$ mJ/mole °K^2, or about twice the value for $2H$-TaS_2. From these superconductivity and heat-capacity data, it is estimated[27] that the phonon enhancement factor $(1+\lambda) \approx 1.6$. Photoemission studies[18] indicate an occupied niobium $4d$ conduction bandwidth of less than 0.7 eV and a selenium $4p$ valence bandwidth of 6–7 eV. From a study of the optical anisotropy in $2H$-$NbSe_2$, Liang[28] has determined a rough estimate of the free-carrier mass anisotropy. He finds room-temperature mass ratios of 5.3 and 3.4 for electron motion parallel and perpendicular to the hexagonal c axis, respectively.

E. $2H$-MoS_2

Although most crystals of the TX_2 layer-type compounds are synthetic, natural MoS_2 crystals with the $2H$ and $3R$ phases are quite common. In 1923, Dickinson and Pauling[29] first determined the crystal structure of $2H$-MoS_2, the mineral molybdenite. Along with the other group-VIB layer compounds, $2H$-MoS_2 samples exhibit semiconducting behavior. There is some disagreement concerning the magnitude of the band gap in $2H$-MoS_2. Wilson and Yoffe[1] attribute a weak indirect edge at 0.2 eV to the semiconducting energy gap. Huisman, DeJonge, Haas, and Jellinek (HDHJ)[9] believe that this 0.2-eV structure is extrinsic and propose that the intrinsic gap in $2H$-MoS_2 is about 1.4 eV. Recent photoemission studies[18,30] suggest that this gap is at least 1 eV. The low-energy optical properties of $2H$-MoS_2 (as well as the other group-VIB compounds) are dominated by a pair of sharp exciton lines. In $2H$-MoS_2, these occur at about 2 eV and are separted by about 0.2 eV.[1,31]

Information about the states near the top of the valence band in $2H$-MoS_2 has been provided by electron paramagnetic resonance studies on As-doped samples.[32] These results suggest that the holes near the valence-band edge involve molybdenum $4d$ wave functions with d_{z^2} symmetry. Somoano *et al.*[33] find that the intercalation compounds which are formed by adding alkali-metal atoms to $2H$-MoS_2 are both metallic and superconducting, with transition temperatures as high as 6.5 °K.

III. COMPUTATIONAL DETAILS

APW programs that were developed earlier for the hexagonal-close-packed (hcp) structure[34] have been modified in this investigation to handle a variety of binary hexagonal compounds, including those with the $C6$, $C27$, and $C7$ crystal structures. The $C27$ and $C7$ structures have the same nonsymmorphic space group (D_{6h}^4) as the hcp structure, so in these cases, the program modification involves primarily changes in the number and location of the atoms in the unit cell. The space group for the $C6$ crystal structure is symmorphic (D_{3d}^3) and includes those symmetry operations in D_{6h}^4 that do not involve nonprimitive translations.[11] Thus, by omitting this class of symmetry operations, one can easily treat the $C6$ structure as a special case of the D_{6h}^4 space group.

As noted previously,[34] the fact that each of the crystal structures which is considered here has an inversion center helps to simplify the APW calculation considerably. If one chooses the origin of coordinates so that it coincides with the inversion center, then the APW energy-overlap matrix can be set up so that it is real rather than complex. With this choice, the structure factors $e^{\pm i\vec{k}\cdot\vec{r}_n}$ that occur in the APW matrix[35] reduce either to 1 or 2 $\cos\vec{k}\cdot\vec{r}_n$, depending on whether the atomic position vector $\vec{r}_n$ is at the origin or not.

In each of the $1T$ and $2H$ phases, the X-atom sites have C_{3v} point symmetry. The symmetry of the T-atom sites is different in the $1T$ and $2H$ phases. In $1T$-HfS_2, the Hf sites have D_{3d} symmetry, whereas in $2H$-TaS_2 and $2H$-MoS_2, the Ta and Mo sites both have D_{3h} symmetry. It is noted that the $C6$ ($1T$-TX_2) phase coincides with the NiAs structure (which also has the D_{6h}^4 space group) if a second T atom is inserted in the Van der Waals gap at $\vec{r}_n = (0, 0, \frac{1}{2})$ and $z = \frac{1}{4}$. The partial filling of these sites produces Phillips's "bridge" compounds.[36]

The present APW calculations involve *ad hoc* crystal potentials that are derived from the Hartree-Fock-Slater atomic charge densities of Herman and Skillman.[37] In each case, the atomic configuration of the metal and chalcogen atoms are assumed to be $d^n s^1$ and $s^2 p^4$, respectively. Slater's original[38] free-electron exchange approximation is used. The methods for calculating the muffin-tin potentials and treating the muffin-tin corrections in the region outside the APW spheres are analogous to those applied previously in similar calculations for ReO_3,[39] the $3d$ monoxides,[40] and several perovskite-type compounds.[41]

The values assumed for the metal- and chalcogen-atom APW sphere radii (R_T and R_X, respectively) are listed in Table III, along with the observed (or assumed) values for the positional parameter z. As in the earlier calculations,[39–41] the values for R_T and R_X are chosen so that the T- and X-atom spheres touch along the nearest-neighbor direction and $R_T/R_X \approx \frac{7}{6}$. It is found that this choice optimizes the convergence of both the T-atom d and the X-atom p energy-band states[35] and minimizes the corrections to the muffin-tin potential in the region between the APW spheres. This table includes an entry for a hypothetical form

TABLE III. APW sphere radii for TX_2 layer compounds.

Type	TX_2	z	R_T(a.u.)	R_X(a.u.)
1T	HfS_2	0.25	2.60	2.23
	TaS_2	0.25	2.47	2.12
2H	TaS_2	0.118	2.53	2.17
	NbSe	0.1163	2.64	2.26
	$NbSe_2$[a]	0.1423	2.64	2.26
2H	MoS_2	0.621	2.46	2.11

[a]Hypothetical compound in which the c axis is expanded from ~12.5 to 15.5 Å to simulate intercalation.

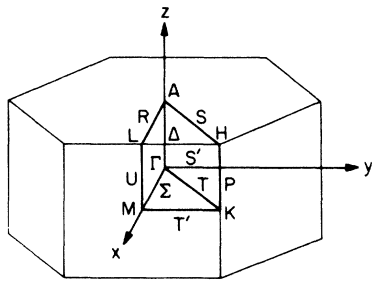

FIG. 2. Brillouin zone for the hexagonal Bravais lattice with symmetry points and lines labeled according to the standard notation.

of 2H-$NbSe_2$ in which the c lattice parameter has been expanded by about 3 Å to simulate in a very crude way the effects of intercalation.

In Table IV we summarize the sandwich heights, interlayer distances, and T-T, X-X, and T-X bond lengths in these compounds. Here, it is shown that the parameter z for the hypothetical form of 2H-$NbSe_2$ in Table III is such that the sandwich height is unchanged and the interlayer separation is increased by about 1.5 Å. We note that the intralayer X-atom bond lengths are not equal, so unlike the earlier band calculations,[4-6] the octahedral or trigonal-prismatic coordination of the metal atoms is slightly distorted rather than "ideal"

The only new feature of the present APW calculations is that they exploit the approximate linear dependence of the logarithmic derivatives on energy for $l \geq 4$ to simplify the APW programs and increase their computational efficiency.[35] Test calculations that apply this linear fit over a 1.6 Ry energy range demonstrate that this approximation yields energy eigenvalues that agree with the standard APW results to better than four decimal places.

The reciprocal lattice vectors for the hexagonal lattice generated by Eq. (1) are given by

$$\vec{b}_1 = (2/\sqrt{3}a)\hat{i}, \quad \vec{b}_2 = (1/\sqrt{3}a)(\hat{i} + \sqrt{3}\hat{j}), \quad \vec{b}_3 = (1/c)\hat{k}. \tag{2}$$

An arbitrary lattice vector in k space can be written

$$\vec{K}_n = 2\pi\,(n_1\vec{b}_1 + n_2\vec{b}_2 + n_3\vec{b}_3), \tag{3}$$

where the n_i are integers. The corresponding Brillouin zone is shown in Fig. 2, where the symmetry points and lines are labeled in accordance with Herring's notation.[42] The scale of the Brillouin zone shown in Fig. 2 corresponds roughly to the c/a ratio for 1T-HfS_2. The corresponding dimensions along the z axis are reduced by about a factor of 2 for the 2H compounds.

As in previous APW calculations for transition-metal compounds.[39-41] the scope of the present study has been limited to high-symmetry points in the Brillouin zone by the large number of APW basis functions that are required to achieve adequate convergence of the energy eigenvalues. The present calculations for the 1T-TX_2 and 2H-TX_2 compounds include approximately 160 and 280 APW basis functions, respectively. It is estimated that these yield energy-band results which are converged to within a few thousandths of a rydberg. The maximum dimensions for the symmetrized APW matrix was arbitrarily set at 60×60, and this proved to be sufficient to achieve satisfactory convergence at the six symmetry points in the

TABLE IV. Tabulation of sandwich heights, interlayer distances, and bond lengths (Å) in TX_2 layer compounds.

Type	TX_2	Sandwich height	Interlayer distance	$d(T$-$X)$	Intralayer $d(X$-$X)$	$d(T$-$T) = d(X$-$X)$	Interlayer $d(X$-$X)$
1T	HfS_2	2.92	2.92	2.56	3.60	3.64	3.60
	TaS_2	2.93	2.93	2.43	3.51	3.37	3.51
2H	TaS_2	3.19	2.85	2.49	3.19	3.32	3.43
	$NbSe_2$	3.34	2.90	2.59	3.34	3.44	3.52
	$NbSe_2$[a]	3.34	4.41	2.59	3.34	3.44	4.84
2H	MoS_2	3.17	2.98	2.42	3.17	3.16	3.49

[a]See Ref. a in Table III.

Brillouin zone (Γ, M, K, A, L, and H). One exception involves the L_1 states in the $2H$ compounds, where convergence errors could be as large as 0.01 Ry. Limited calculations were performed along symmetry lines. These usually involved fewer than the optimum number of APW basis functions, expecially in the ALH plane where only a subgroup of the full wave-vector group is utilized in the symmetrized calculations.[34]

The character tables for the D_{6h}^4 space group were first worked out by Herring.[42] Slater[11] has tabulated the irreducible representations for both the D_{3d}^3 and D_{6h}^4 space groups. In the case of the D_{6h}^4 space group, Slater's notation agrees with that of Herring if the H_2 and H_3 irreducible representations are interchanged. The present notation includes this interchange and is therefore consistent with Herring's original notation.

The D_{6h}^4 space group is nonsymmorphic. With the origin of coordinates at the inversion center,[11] those space-group operations $\{\alpha \mid \vec{R}_n\}$ whose rotational parts α are included in the D_{3d} point group are associated only with primitive translations $\vec{R}_n = n_1\vec{t}_1 + n_2\vec{t}_2 + n_2\vec{t}_3$, where n_i are integers and the $\vec{t}_i$ are given by Eq. (1). The remaining twelve space-group operations have the form $\{\alpha \mid \vec{R}_n + \vec{\tau}\}$, where the nonprimitive translation $\vec{\tau} = \frac{1}{2}\vec{t}_3 = \frac{1}{2}c\hat{k}$. For ease in programming the symmetrized APW method so that it can be applied to both the D_{3d}^3 and D_{6h}^4 space groups, it is convenient to order these symmetry operations in such a way that the twelve D_{3d} point-group operations have odd indices and the remaining operations have even indices. One can then arrange to include or skip the even operations, and thereby treat either the D_{6h}^4 or D_{3d}^3 space groups in a systematic manner.

The notation adopted here for the D_{3d}^3 irreducible representations is identical with that of Murray *et al.*[4] This notation coincides with that introduced by Fong and Cohen[43] if the + superscripts are ignored and the − superscripts are replaced by primes.

Using standard group-theoretical techniques, we have determined the symmetry properties of Bloch sums formed from s, p, and d orbitals localized about the T and X sites in both the $1T$-TX_2

TABLE V. Symmetry properties of Bloch sums formed from s, p, and d orbitals at the metal and sulfur sites in $1T$-HfS_2, $2H$-TaS_2, and $2H$-MoS_2.

(a) $1T$-HfS_2	Γ	M	K	A	L	H
Hf s	1^+	1^+	1	1^+	1^+	1
p_z	2^-	2^-	2	2^-	2^-	2
p_x, p_y	3^-	1^-, 2^-	3	3^-	1^-, 2^-	3
d_{z^2}	1^+	1^+	1	1^+	1^+	1
d_{xy}, $d_{x^2-y^2}$	3^+	1^+, 2^+	3	3^+	1^+, 2^+	3
d_{xz}, d_{yz}	3^+	1^+, 2^+	3	3^+	1^+, 2^+	3
S s	1^+, 2^-	1^+, 2^-	3	1^+, 2^-	1^+, 2^-	3
p_z	1^+, 2^-	1^+, 2^-	3	1^+, 2^-	1^+, 2^-	3
p_x, p_y	3^+, 3^-	$1^\pm$, $2^\pm$	1, 2, 3	3^+, 3^-	$1^\pm$, $2^\pm$	1, 2, 3
(b) $2H$-TaS_2						
Ta s	1^+, 4^-	1^+, 2^-	1, 3	1	1	1
p_z	3^+, 2^-	3^+, 4^-	2, 4	1	1	1
p_x, p_y	5^+, 6^-	1^+, 4^+, 2^-, 3^-	5, 5	3	1, 2	2, 3
d_{z^2}	1^+, 4^-	1^+, 2^-	1, 3	1	1	1
d_{xy}, $d_{x^2-y^2}$	5^+, 6^-	1^+, 4^+, 2^-, 3^-	5, 5	3	1, 2	2, 3
d_{xz}, d_{yz}	6^+, 5^-	2^+, 3^+, 1^-, 4^-	6, 6	3	1, 2	2, 3
S s	1^+, 3^+, 2^-, 4^-	1^+, 3^+, 2^-, 4^-	5, 6	1, 1	1, 1	2, 3
p_z	1^+, 3^+, 2^-, 4^-	1^+, 3^+, 2^-, 4^-	5, 6	1, 1	1, 1	2, 3
p_x, p_y	$5^\pm$, $6^\pm$	$1^\pm$, $2^\pm$, $3^\pm$, $4^\pm$	1, 2, 3, 4, 5, 6	3, 3	1, 1, 2, 2	1, 1, 2, 3
(c) $2H$-MoS_2						
Mo s	1^+, 4^-	1^+, 2^-	5	1	1	3
p_z	3^+, 2^-	3^+, 4^-	6	1	1	2
p_x, p_y	5^+, 6^-	1^+, 4^+, 2^-, 3^-	1, 3, 5	3	1, 2	1, 2
d_{z^2}	1^+, 4^-	1^+, 2^-	5	1	1	3
d_{xy}, $d_{x^2-y^2}$	5^+, 6^-	1^+, 4^+, 2^-, 3^-	1, 3, 5	3	1, 2	1, 2
d_{xz}, d_{yz}	6^+, 5^-	2^+, 3^+, 1^-, 4^-	2, 4, 6	3	1, 2	1, 3
S s	1^+, 3^+, 2^-, 4^-	1^+, 3^+, 2^-, 4^-	5, 6	1, 1	1, 1	2, 3
p_z	1^+, 3^+, 2^-, 4^-	1^+, 3^+, 2^-, 4^-	5, 6	1, 1	1, 1	2, 3
p_x, p_y	$5^\pm$, $6^\pm$	$1^\pm$, $2^\pm$, $3^\pm$, $4^\pm$	1, 2, 3, 4, 5, 6	3, 3	1, 1, 2, 2	1, 1, 2, 3

and $2H$-TX_2 compounds. The results of this analysis at the six symmetry points in the Brillouin zone are included in Table V. For each structure, we identify the appropriate irreducible representation by its subscript. Thus, the entries 1^+ and 2^- at the point M denote the M_{1^+} and M_{2^-} irreducible representations, respectively. Duplicate entries indicate that the same representation occurs twice within a given set of Bloch functions. Sine the D_{3d}^3 and D_{6h}^4 space groups contain a unique z axis, we subdivide the p functions into those with p_z and p_x, p_y symmetry. In the case of the d functions, a similar separation results in three groups, including (a) d_{z^2}; (b) d_{xy}, $d_{x^2-y^2}$; (c) d_{xz}, d_{yz}. These results are useful for identifying the atomic symmetry of particular bands or groups of bands in the following sections.

IV. APW RESULTS

A. 1T-HfS_2 and 1T-TaS_2

The APW results for the 1T-phase HfS_2 and TaS_2 compounds are shown in Figs. 3 and 4, respectively. The results of the APW calculations are indicated with open circles and the band profiles are rough estimates that are determined to a large extent by the compatibility relations.[43] In both compounds, the lower group of six bands are derived primarily from the sulfur $3p$ orbitals. In 1T-HfS_2, these are separated by an 0.2-Ry gap from the empty hafnium $5d$ bands. The dashed bands in the upper portion of Fig. 3 correspond to the bottom of the hafnium $6s$-$6p$ bands. A similar ordering of bands is found in 1T-TaS_2, though in this case, the $3p$-$5d$ band separation is reduced

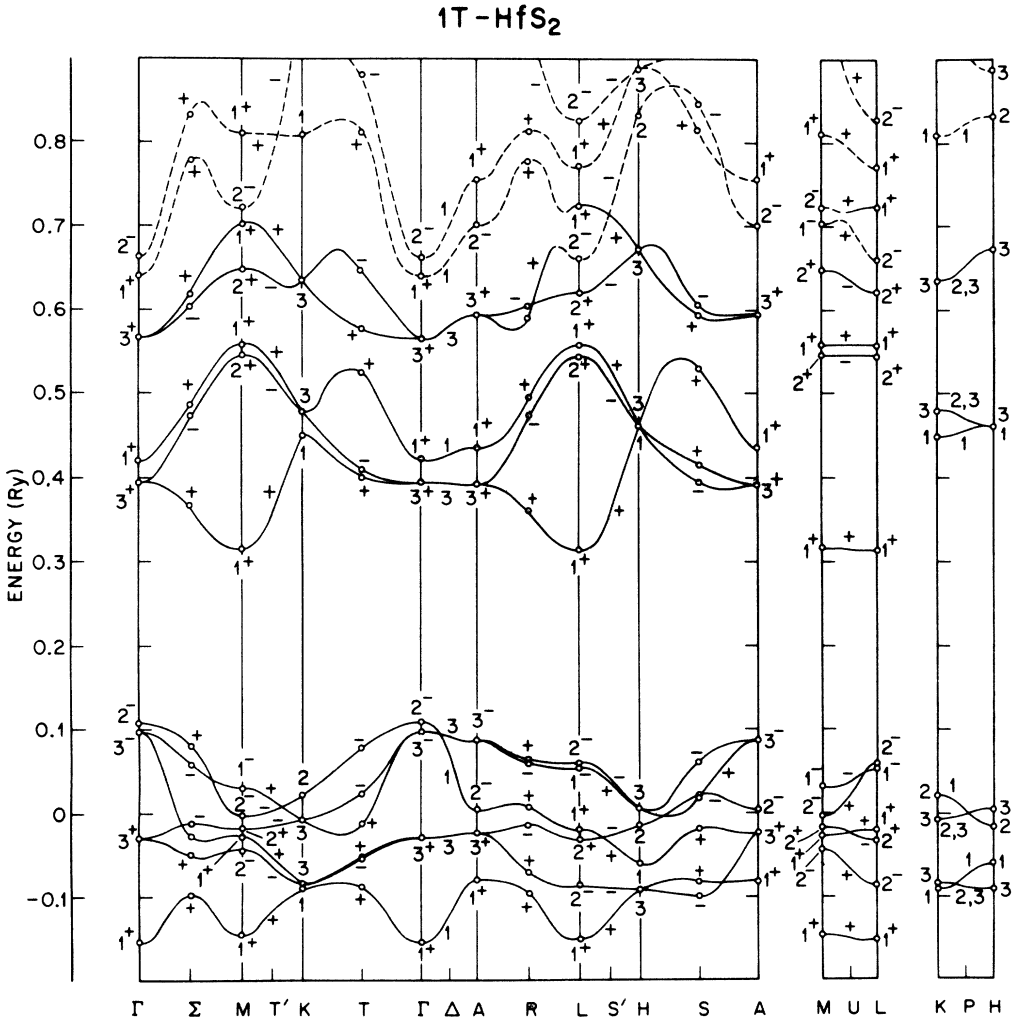

FIG. 3. APW energy-band results (open circles) for 1T-HfS_2. Energies are relative to the muffin-tin constant, $V_0 = -0.842$ Ry.

to about 0.1 Ry and the Fermi-level (indicated by the dashed horizontal line) now lies in the lower portion of the tantalum 5*d* bands. The energy scale for these (as well as the following) results is such that the muffin-tin constant is zero.

It is found that the 5*d* bands in these octahedrally coordinated compounds are split into nonoverlapping subbands. Based on tight-binding arguments that are described in Sec. V, we identify the 5*d* orbitals associated with the lower triply degenerate subband as those with d_{z^2}, d_{xy}, and $d_{x^2-y^2}$ type symmetry and refer to this lower manifold as the t_{2g} subband. Because of the close proximity of the dashed metal 6*s*-6*p* bands in Figs. 3 and 4, hybridization effects blur the actual width of the upper doubly degenerate e_g subband formed from the d_{xz} and d_{yz} orbitals. We arbitrarily associate the lowest states with the correct symmetry to these d_{xz} and d_{yz} orbitals. This leads to t_{2g} (e_g) bandwidths of 0.25 (0.15) and 0.30 (0.20) Ry in 1*T*-HfS_2 and 1*T*-TaS_2, respectively. The larger sulfur 3*p* and tantalum 5*d* bandwidths in 1*T*-TaS_2 are due undoubtedly to increased overlap-covalency effects that result from the smaller lattice parameter in the basal plane (see Table II).

The differences between the energy-band results in the ΓMK and ALH planes in Figs. 3 and 4 are due to interlayer interactions. Within the sulfur 3*p* and metal 5*d* manifolds, these bandwidths are usually less than 0.05 Ry. Two noticeable exceptions involve the bands joining the Γ_2^-, A_2^-, and Γ_1^+, A_1^+ states within the 3*p* manifold. This is not surprising, since according to Table V, these states correspond to sulfur p_z orbitals for which significant interlayer coupling is expected.

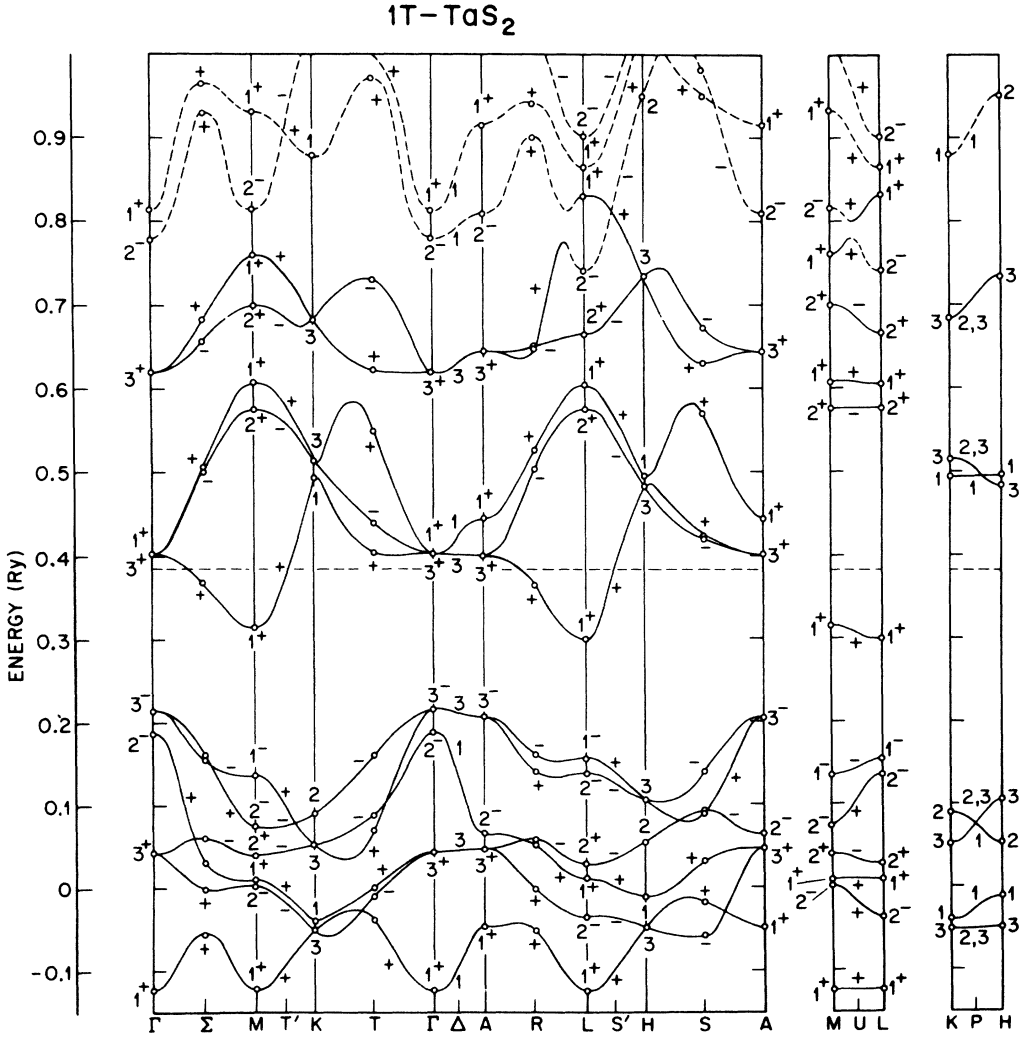

FIG. 4. APW results for 1*T*-TaS_2, where $V_0 = -0.945$ Ry.

B. $2H$-$NbSe_2$ and $2H$-TaS_2

The corresponding APW results for the group-VB $2H$ compounds TaS_2 and $NbSe_2$ are shown in Figs. 5 and 6, respectively. It is clear that these results are considerably more complicated than those for the $1T$ phase, mainly because the number atoms in the unit cell has doubled. In both compounds, the lowest group of twelve bands evolve from X-atom p orbitals. Above these, we find the ten metal d bands, and finally, near the top of each figure, the (dashed) metal s-p bands. In each compound, the ten metal d bands are split by a gap of about 0.1 Ry into a lower pair of d subbands and a group of eight d bands at higher energies. In these group-VB compounds, the dashed Fermi level occurs within this lower splitoff d subband, thereby predicting metallic behavior for these materials. As we shall show in Sec. IV C, the group-VIB compounds such as $2H$-MoS_2 possess a similar band structure. In this case, the lower d subband is completely filled and this leads to semiconducting behavior in the group-VIB compounds.

At first sight, these results appear to be consistent with the Wilson-Yoffe model,[1] which contains a nonbonding d_{z^2} subband that is partially filled in $2H$-TaS_2 and $2H$-$NbSe_2$ and totally filled in $2H$-MoS_2. However, we note from the results of Table V that, while the lowest subband contains d_{z^2} type orbitals at Γ, it has the symmetry of d_{xy}, $d_{x^2-y^2}$ orbitals at K. The d_{z^2} subband actually extends up to K_1, K_3, the lowest pair of bands at K in the upper d complex. In terms of a tight-binding model that is described in Sec. V, we show that strong hybridization between the d_{z^2} and d_{xy}, $d_{x^2-y^2}$ subbands is responsible for the 0.1 – Ry energy gap that exists within the d manifold of these $2H$ compounds. Thus, the small (0.075 Ry) width of the lowest subband is an artifact of this hybridization gap and is not to be interpreted as a measure of the strength of the metal-chalcogen s-d or p-d interactions or the direct metal-metal d-d interactions.

Because of the additional symmetry of the D_{6h}^4 space group, a double degeneracy exists everywhere in the ALH plane when spin-orbit coupling is neglected.[34] As in the case of the $1T$ compounds, the bandwidths along the Δ, U, or P lines of the Brillouin zone reflect the strength of the interlayer interactions. Among the metal d-band states, these are largest for the d_{z^2} orbitals (Γ_1^+, A_1; Γ_4^-,

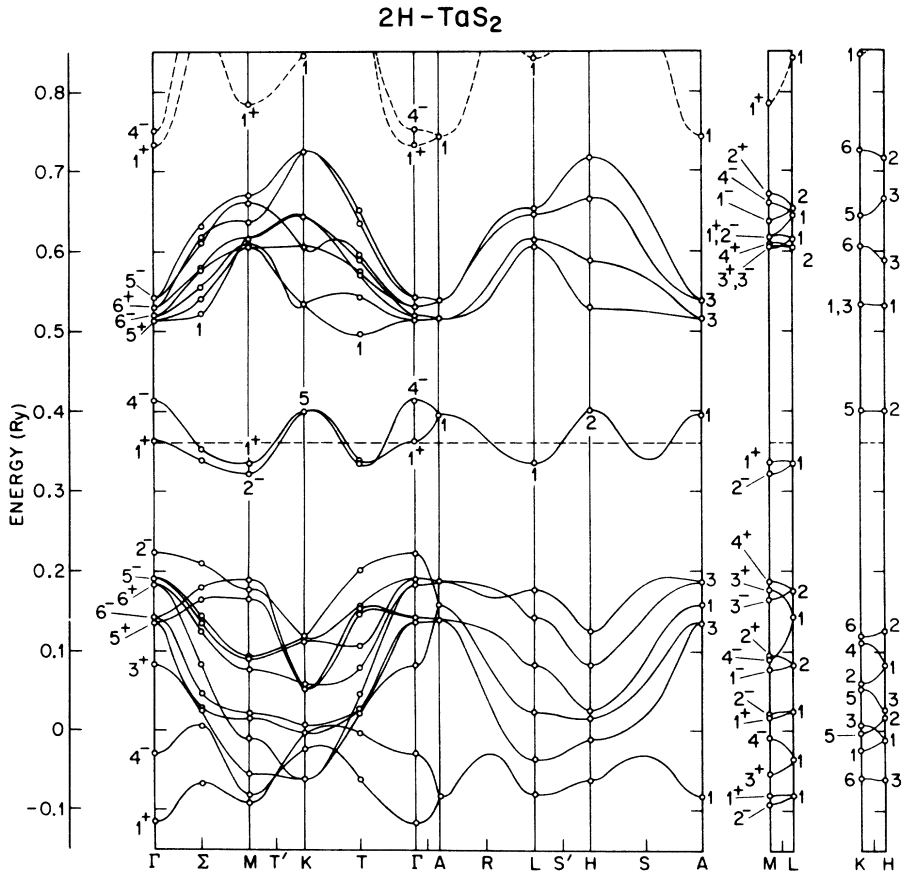

FIG. 5. APW results for $2H$-TaS_2, where $V_0 = -0.938$ Ry.

A_1). Within the chalcogen p manifold, the bands associated with the p_z-type orbitals (Γ_{2-}, A_1; Γ_{3+}, A_1; Γ_{4-}, A_1; Γ_{1+}, A_1) again reflect rather substantial interlayer interactions.

To help distinguish between the interlayer and intralayer contributions to the band profiles, we show in Fig. 7 the energy-band results for " intercalated" 2H-$NbSe_2$. As discussed previously (see Tables III and IV), this calculation involves a hypothetical form of 2H-$NbSe_2$ in which the interlayer separation is increased by about 1.5 Å. It is clear from a comparison of the results shown in Figs. 6 and 7 that the interlayer interactions are substantially reduced in the latter calculation. It is noted that the energy scales for the two 2H-$NbSe_2$ calculations will nearly coincide if those in Fig. 7 are shifted by 0.189 Ry; this is in fact the difference in the values of the corresponding muffin-tin constants. In Fig. 7, it is found that the bands in the ΓMK and ALH planes are nearly identical, so that the band structure is nearly that of a two-dimensional compound.

C. 2H-MoS_2

The APW results for 2H-MoS_2 are shown in Fig. 8. Neglecting interlayer interactions, 2H-MoS_2 has the same two-dimensional crystal structure as the group-VB 2H compounds. Therefore, it is not surprising that the band structures for these two groups are similar. According to Table V, some changes take place in the symmetry properties of metal s, p, and d bands at the K and H points, and these are reflected in the results shown in Fig. 8. We note that the lowest pair of d bands at K now has K_1-K_3 symmetry, so it still corresponds to d_{xy}, $d_{x^2-y^2}$ type orbitals. Although there are now two K_5 states in the upper d manifold, a comparison with the results for the group-VB compounds and the analysis in Sec. V suggests that the lower one corresponds to the d_{z^2} orbitals. Thus, these results predict an 0.085-Ry indirect gap that results from intralayer hybridization between the d_{z^2} and d_{xy}, $d_{x^2-y^2}$ subbands.

D. Sulfur 3s and Selenium 4s Core States

We have calculated the sulfur 3s bands in 2H-TaS_2 and the selenium 4s bands in 2H-$NbSe_2$. In the former compound, these bands have a width of 0.12 Ry and are centered about an energy of −0.7 Ry on the energy scale of Fig. 5. In the case of $NbSe_2$ (Fig. 6), the selenium 4s bands are slightly broader (0.13 Ry) and slightly higher in energy

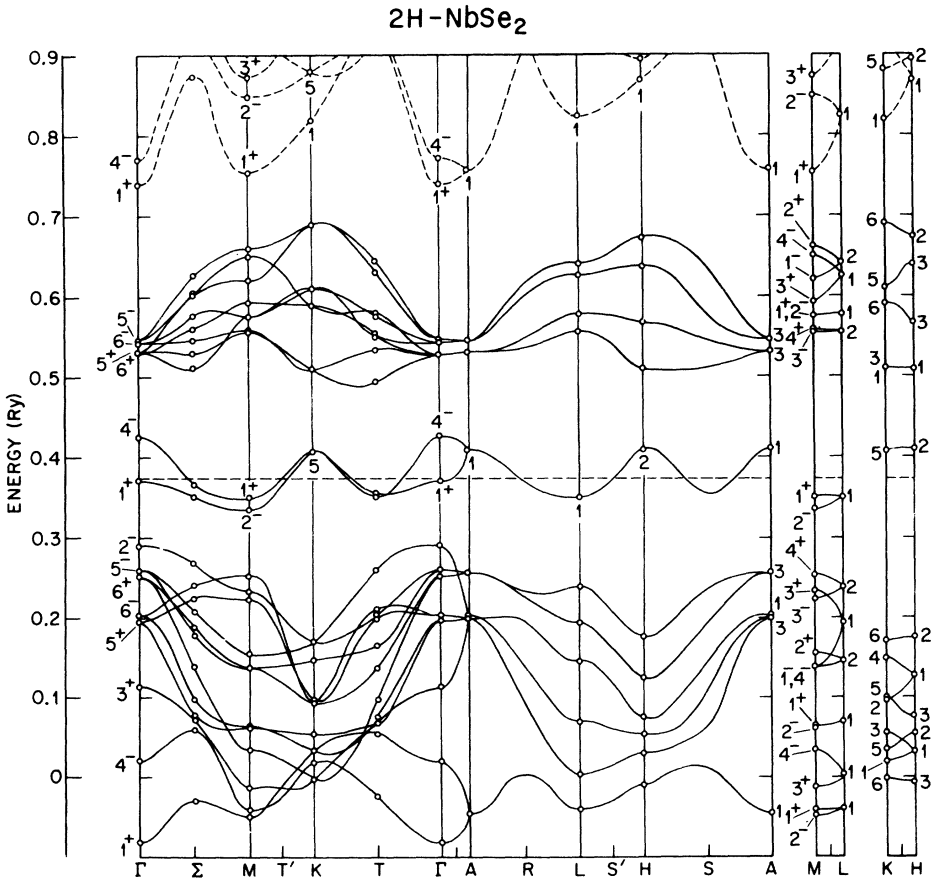

FIG. 6. APW results for 2H-$NbSe_2$, where $V_0 = -0.931$ Ry.

(−0.65 Ry) relative to the muffin-tin constant. Thus, it is expected that the X-atom s bands will lie about 0.9 Ry below the top of the p bands in both the sulfides and the selenides. This is reasonably close to the 0.8 Ry difference between the atomic $3s$ ($4s$) and $3p$ ($4p$) levels in sulfur (selenium).[37]

E. Muffin-Tin Corrections

To illustrate the effect of the muffin-tin corrections on the present APW results, we compare in Table VI the APW muffin-tin (MT) eigenvalues at Γ for $1T$-TaS_2 and $2H$-$NbSe_2$ with those obtained when the corrections between the APW spheres are included (muffin-tin corrections). It is found that individual eigenvalues change by as much as ±0.08 Ry. It is believed that two competing mechanisms combine to produce these changes. The gross features of these results can be understood by considering the nature of these muffin-tin corrections.

In the muffin-tin approximation, the constant V_0 is chosen so that the average potential in the region outside the APW spheres is zero. As a result, the corrections are found to be negative in the regions just outside the T- and X-atom spheres and positive in the more remote corners of the unit cell. Thus, one effect of these corrections is to lower the energies of both the semilocalized metal d-type and chalcogen p-type states whose charge densities are concentrated primarily in those regions where the muffin-tin corrections are negative. The wave functions of the more extended metal s-p states correspond to a more uniform charge density, one that extends into the corners of the unit cell. In this case, the corrections can be either positive or negative, depending on

TABLE VI. APW eigenvalues at Γ for $1T$-TaS_2 and $2H$-$NbSe_2$ in the muffin-tin approximation (MT) and including muffin-tin corrections (MTC).

	$1T$-TaS_2			$2H$-$NbSe_2$	
State	MT (Ry)	MTC (Ry)	State	MT (Ry)	MTC (Ry)
Γ_{1+}	−0.070	−0.123	Γ_{1+}	−0.033	−0.082
Γ_{1+}	0.446	0.403	Γ_{1+}	0.395	0.371
Γ_{1+}	0.731	0.816	Γ_{1+}	0.716	0.740
Γ_{3+}	0.127	0.044	Γ_{3+}	0.120	0.114
Γ_{3+}	0.480	0.402	Γ_{3+}	0.878	0.937
Γ_{3+}	0.655	0.622	Γ_{5+}	0.254	0.197
Γ_{2-}	0.249	0.189	Γ_{5+}	0.555	0.532
Γ_{2-}	0.804	0.780	Γ_{6+}	0.298	0.251
Γ_{3-}	0.276	0.216	Γ_{6+}	0.559	0.531
			Γ_{2-}	0.349	0.290
			Γ_{2-}	0.875	0.905
			Γ_{1-}	0.104	0.020
			Γ_{4-}	0.459	0.427
			Γ_{1-}	0.780	0.771
			Γ_{5-}	0.309	0.259
			Γ_{5-}	0.579	0.547
			Γ_{6-}	0.261	0.203
			Γ_{6-}	0.567	0.543

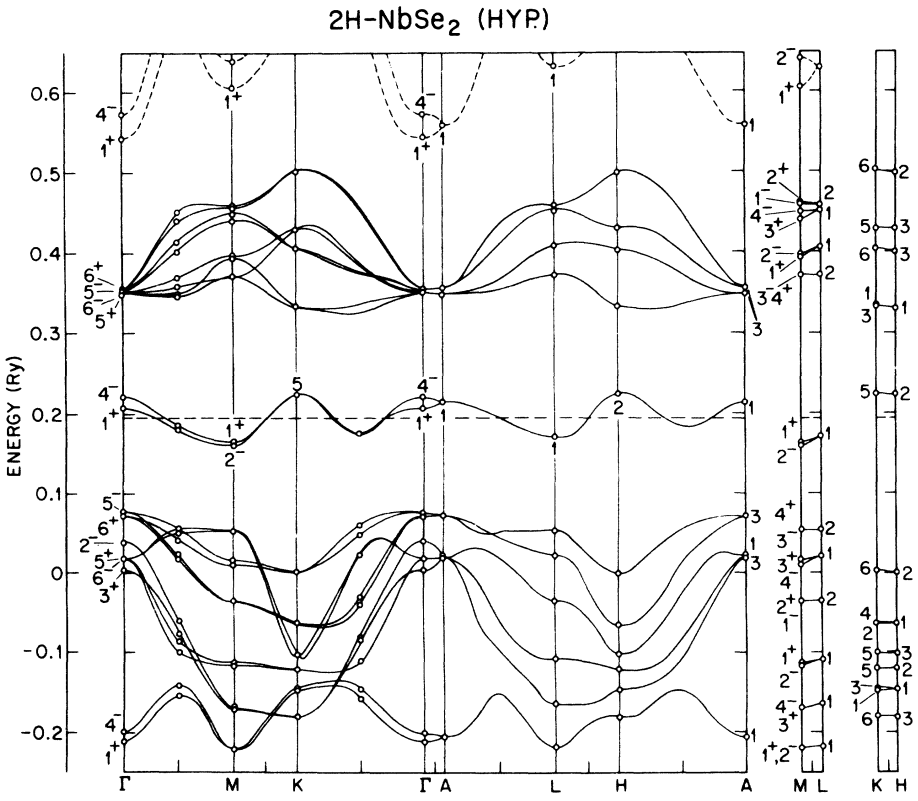

FIG. 7. APW results for a hypothetical form of $2H$-$NbSe_2$ in which the interlayer separation is increased by 1.5 Å ($V_0 = -0.742$ Ry.)

the symmetry of the wave function.

The second mechanism involves metal-chalcogen overlap-covalency effects. The muffin-tin corrections lower the potential barriers along the nearest-neighbor metal-chalcogen bond directions. This enchances the formation of metal-chalcogen σ and π bonds involving the chalcogen s-p and the metal s-p-d orbitals. This enhancement in the strength of the metal-chalcogen bonds causes the energies of the bonding (primarily chalcogen s-p) states to be further lowered but raises the energies of the corresponding antibonding (metal s-p-d) states.

V. TIGHT-BINDING INTERPRETATION

The present energy-band results for the layer-type TX_2 compounds possess many of the same general characteristics as those found previously for the cubic transition-metal oxides.[39–41] An important feature shared by all of these compounds is the fact that the metal s-p bands lie well above the Fermi level. As emphasized earlier,[40,44] this is caused by strong overlap and covalent-bonding effects between the metal and chalcogen s-p orbitals. This results in the formation of metal-chalcogen bonding and antibonding s-p states, with the energy of the latter increased by 5–10 eV. The energy separation between the bonding and antibonding s-p orbitals is generally referred to as the σ-σ^* gap.[1,8] Thus, while the valence bands in Figs. 3–8 are often described as chalcogen p (or s) bands, they are more properly identified as bonding combinations of both metal and chalcogen s-p orbitals. The dashed bands in the upper parts of Figs. 3–8 are antibonding combinations of these same orbitals.

There are similar but weaker overlap-covalency interactions between the metal d and chalcogen s-p orbitals. Unlike the transition metals where the s-p and d bands overlap, the metal d bands usually fall within the σ-σ^* gap in the transition-metal compounds. Except perhaps in the case of the rocksalt structure,[40] these overlap-covalency effects are primarily responsible for the d bandwidth and topology in such compounds.

In order to provide additional insight into the nature of the d-band states in the present $1T$- and $2H$-TX_2 compounds, we apply the Slater and

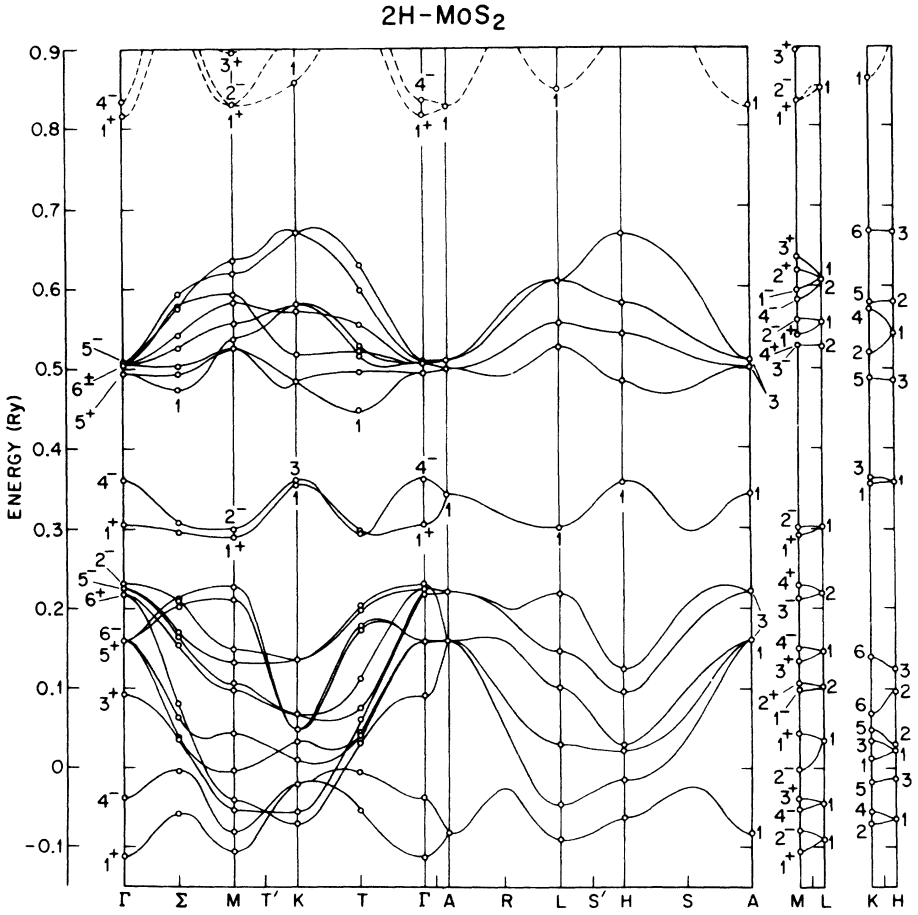

FIG. 8. APW results for $2H$-MoS_2, where $V_0 = -0.961$ Ry.

Koster[45] linear-combination-of-atomic-orbitals (LCAO) interpolation method to fit the APW d-band results of Figs. 3–8. The LCAO matrix elements for the molybdenum $4d$ bands in $2H$-MoS_2 are available from the work of Egorov *et al.*[46] and Miasek.[47] The corresponding LCAO d-band Hamiltonian matrices for the $1T$-TaS_2 and $2H$-TaS_2 structures are easily derived using the group-theoretical techniques of Egorov *et al.*[46]

As discussed previously in the case of the rock-salt structure,[40] the application of the Slater–Koster LCAO interpolation method to fit the d bands in a transition-metal compound where overlap-covalency effects are substantial yields "effective" LCAO parameters $\mathcal{E}_{\alpha,\beta}(\vec{r}_n)$. These effective parameters contain a direct d-d interaction term $E_{\alpha,\beta}(\vec{r}_n)$ between an α orbital at the origin and a β orbital at $\vec{r}_n$ as well as indirect terms (i.e., additional contributions to the d bandwidth that result from overlap-covalency interactions involving the metal d and neighboring chalcogen s-p orbitals).

In the present LCAO fit to the d bands for the $C6$ and $C7$ structure types (Table I), both nearest-neighbor intralayer and interlayer d-d interactions are included. In the case of the $C27$ structure, these are supplemented by a few second-neighbor interlayer interactions. The need for the latter is clear from the results shown in Figs. 5 and 6 as well as those in Table I. In Figs. 5 and 6, it is found that the interlayer splitting of the d_{z^2} bands is much greater at Γ (Γ_{4^-}, Γ_{1^+}) than it is at K (K_1, K_3). According to Table I, nearest-neighbor interlayer d-d interactions produce a splitting within the d_{z^2} subband that is constant throughout the ΓMK plane so that any dependence of this splitting on k_x and k_y must arise from second-neighbor interlayer effects.

The centers of gravity of the various (covalently mixed) d subbands are given by the effective one-center LCAO orbital energies $\mathcal{E}_{\alpha,\alpha}$ (0, 0, 0). These energies are equivalent to the molecular-orbital or ligand-field one-electron levels of an isolated transition-metal complex.[40,44] where the effects of the lattice periodicity are ignored. Consequently, they provide a useful means for comparing the band and ligand-field models for these TX_2 compounds.

A. Band versus Ligand-Field Models

Previous attempts to describe the electronic structure of the TX_2 layer-type compounds have involved either band[1–7] or ligand-field[8,9] models. Although the former method undoubtedly provides the correct description of the electronic states in the present compounds, it is nevertheless useful to compare the present results for the metal d-band states in both the band and ligand-field limits.

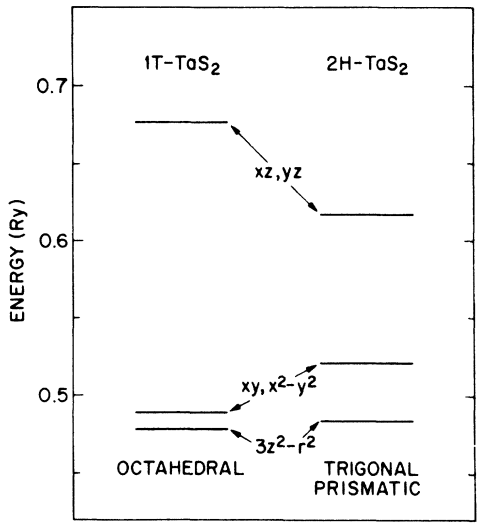

FIG. 9. Comparison between the ligand-field d levels for octahedral and trigonal-prismatic TaS_6 complexes, as derived from the present energy-band results for $1T$-TaS_2 and $2H$-TaS_2, respectively.

It is important to emphasize that the ligand-field levels correspond to the centers of gravity of the appropriate d subbands in the periodic crystal and not (as is often assumed[8]) to the band energies at $\vec{k}=0$.

HDHJ[9] have analyzed a simplified model for the ligand-field splitting of d levels in both octahedral and trigonal-prismatic environments. According to their results, the d-type ligand-field levels for an ideal octahedral TX_6 complex include a lower triply-degenerate t_{2g} level [$\mathcal{E}_{\alpha,\alpha}(0,0,0)$ with $\alpha = z^2$, xy, and x^2-y^2 in the present coordinate system] and an upper doubly degenerate e_g state ($\alpha = xz$, yz). In the case of a trigonal-prismatic TX_6 complex, their results show that the octahedral t_{2g} level is split into a singly degenerate ($\alpha = z^2$) and a doubly-degenerate ($\alpha = xy$, x^2-y^2) level.

In Fig. 9 we compare the ligand-field splittings of the $5d$ levels in $1T$-TaS_2 (octahedral) and $2H$-TaS_2 (trigonal-prismatic), as determined by the present APW-LCAO method. These represent the centers of gravity of the various d subbands shown in Figs. 4 and 5, respectively. These ligand-field results are in excellent agreement with those shown in Fig. 3 of the paper by HDHJ.[9] The existence of a small splitting between the d_{z^2} and d_{xy}, $d_{x^2-y^2}$ levels in Fig. 9 for the octahedral coordination is consistent with the fact that the present calculation for $1T$-TaS_2 involves a slightly distorted octahedron with edges of 3.37 and 3.51 Å, respectively.

A second similarity between the present results and those of HDHJ concerns the fact that the split-

ting between the d_{xz}, d_{yz}, and d_{z^2} levels is smaller in the case of the trigonal prism than it is for the octahedral TX_6 complex. In the trigonal-prismatic complex, the ordering of the d_{z^2} and d_{xy}, $d_{x^2-y^2}$ levels agrees with that proposed by HDHJ,[9] but is opposite to that of Goodenough.[8]

Finally, we note that the 0.1 Ry hybridization gap within the tantalum 5*d* manifold in 2*H*-TaS_2 (Fig. 5) is larger than and not related directly to the 0.04-Ry ligand-field splitting between the d_{xy}, $d_{x^2-y^2}$ and d_{z^2} levels shown in the right-hand portion of Fig. 9. HDHJ[9] assume that this ligand-field splitting must be at least 1.4 eV in 2*H*-MoS_2 in order to explain the observed optical gap. Goodenough's model[8] involves a somewhat larger splitting since he assumes a reversed order for the d_{xy}, $d_{x^2-y^2}$, and d_{z^2} levels and assigns the optical gap to the spin-orbit split d_{xy}, $d_{x^2-y^2}$ level. The corresponding APW-LCAO results for 2*H*-MoS_2 yield a ligand-field splitting between the d_{xy}, $d_{x^2-y^2}$, and d_{z^2} levels of 0.045 Ry, which is about one-half the 0.09-Ry hybridization gap shown in Fig. 8.

It is useful to apply these techniques to compare the gross features of the present APW-LCAO results for the group-IV*B* and group-VI*B* compounds with the semiempirical band structures of Bromley, Murray and Yoffe (BMY).[2-6] For example, while MBY[4] assume ideal octahedral coordination in their calculation for 1*T*-HfS_2, the corresponding energy-band results suggest an 0.1-Ry splitting between the centers of gravity of the d_{z^2} and d_{xy}, $d_{x^2-y^2}$ subbands. This is about ten times larger than the present APW-LCAO estimate of 0.01 Ry for this splitting in 1*T*-HfS_2. A similar discrep-

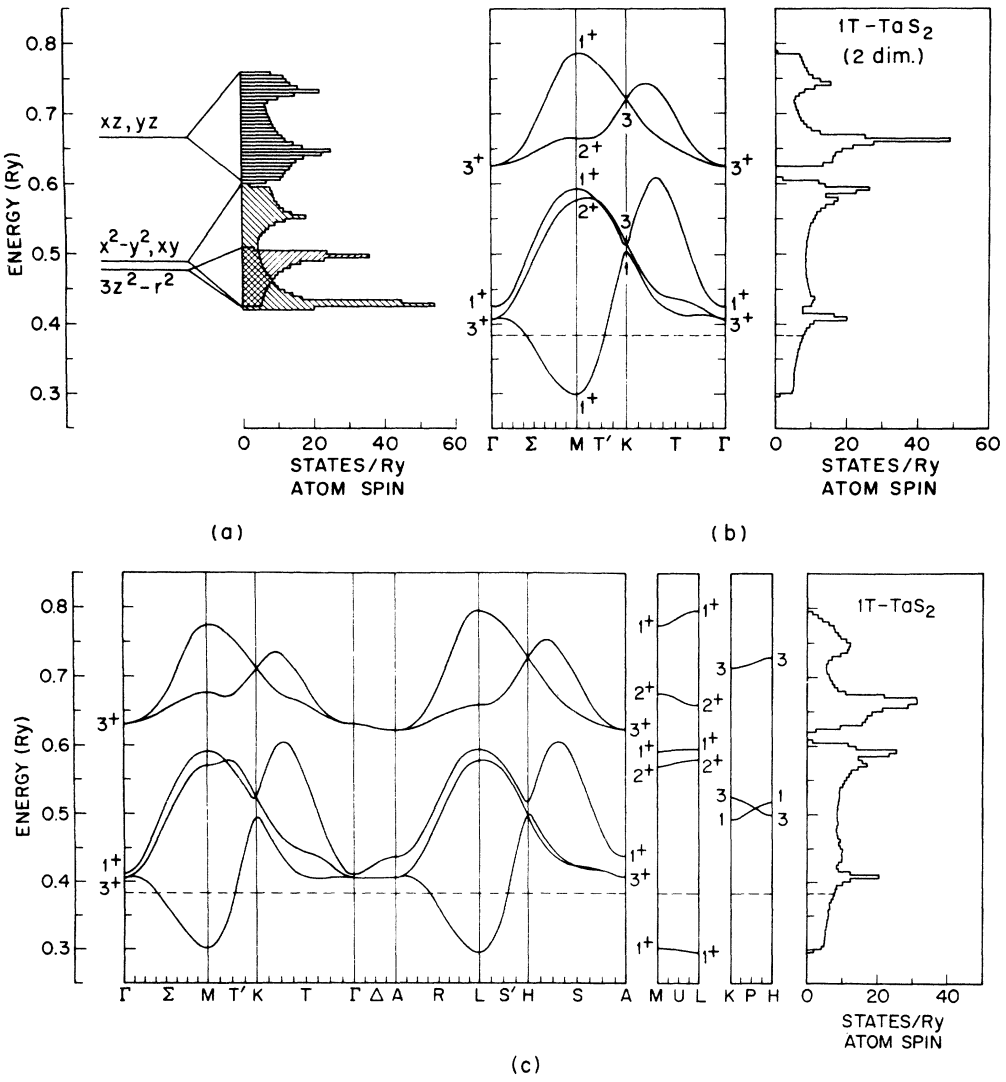

FIG. 10. (a) Ligand-field levels and LCAO density-of-states curves for unhybridized *d* bands in 1*T*-TaS_2. LCAO results for 1*T*-TaS_2 with hybridization, first neglecting (b) and then including (c) interlayer interactions.

ancy is found in the results for $2H$-MoS_2. In this case, the results of BMY[5] suggest an 0.12-Ry splitting between the d_{xy}, $d_{x^2-y^2}$, and d_{z^2} levels whereas the present APW-LCAO estimate is about one-third as large.

B. LCAO D Bands

We now apply this LCAO model to trace the manner in which the various d subbands evolve in these $1T$-TX_2 and $2H$-TX_2 compounds when the effects of the lattice periodicity are taken into account. By setting the effective d-d parameters $\mathcal{E}_{\alpha,\beta}(\vec{r}_n)$ for interlayer interactions equal to zero, we can determine the "two-dimensional" band structures for these materials. In addition, by either omitting or including various d-d hybridization parameters [such as $\mathcal{E}_{\alpha,\beta}(\vec{r}_n)$ with $\alpha = z^2$ and $\beta = xy$ or x^2-y^2], we can indicate rather graphically the importance of interband hybridization effects in determining the APW energy-band results for these compounds.

The LCAO results for the tantalum $5d$ bands in $1T$-TaS_2 are shown in Fig. 10. The results shown in Figs. 10(a) and 10(b) neglect interlayer interactions. In Fig. 10(a) we relate the ligand-field levels to the density-of-states curves for the corresponding d subbands, neglecting interband hybridization. The effects of hybridization on the $E(\vec{k})$ and density-of-states curves are shown in Fig. 10(b). Finally in Fig. 10(c) the corresponding results for three-dimensional $1T$-TaS_2 are shown. By comparing these results with those in Fig. 10(b), one concludes that interlayer interactions play a relatively minor role in smearing the sharp singularities that occur in the two-dimensional density-of-states curve.

Similar APW-LCAO results for the d bands in $2H$-MoS_2 are shown in Fig. 11. Again, the histograms joining the various ligand-field levels in Fig. 11(a) represent the density-of-states curves for the individual molybdenum $4d$ subbands, neglecting interband hybridization and interlayer interactions. The corresponding $E(\vec{k})$ and total density-of-states curves are shown to the right. The dashed Fermi level indicates that $2H$-MoS_2 would be metallic in this approximation. The labeling of these two-dimensional energy-band states is in accordance with the notation of BMY.[5] We note that the widths of the various $4d$ subbands in $2H$-MoS_2 are comparable to those in $1T$-TaS_2 when interband hybridization is omitted.

The effect of including interband hybridization is illustrated in Fig. 11 (b). In this two-dimensional limit, reflection symmetry in the basal plane permits hybridization only between the (effective) d_{xy}, $d_{x^2-y^2}$, and d_{z^2} orbitals. According to Fig. 11(b), these hybridization effects result in the formation of a narrow d subband which is half-filled in the group-VB $2H$-TX_2 compounds and completely filled in $2H$-MoS_2. The additional effect of including interlayer interactions is shown in Fig. 11(c).

Similar $E(\vec{k})$ and density-of-states results for three-dimensional $2H$-TaS_2 and $2H$-$NbSe_2$ are contained in Figs. 12(a)–12(c). In each case, the Fermi level occurs quite close to a slightly rounded logarithmic-type singularity in the conduction-band density-of-states curve. For convenience, the energy scale in Fig. 12(c) has been adjusted so that it coincides with that in Fig. 12(b).

A comparison between the LCAO results in Figs. 10–12 and the corresponding APW results in Figs. 4–8 reveals some qualitative as well as quantitative differences, particularly in the band profiles within the upper d-band complexes. The source of these differences is not fully understood, though they may be due to s-d hybridization. In any case, the object of this simplified LCAO model is to achieve a qualitative understanding of the present APW results for the metal d bands. To achieve increased accuracy, one must include explicitly the chalcogen s-p orbitals in the LCAO basis set.[39–41,44]

VI. DISCUSSION

Previous experience with the APW method suggests that this technique is particularly accurate in representing the internal structure of the d bands in transition metals and compounds. However, it is found that such calculations are somewhat less reliable in predicting the relative energies of the s-p and d bands in the transition metals or the correct ligand-metal p-d band separation in transition-metal compounds. As is well known, these aspects of a band calculation are particularly sensitive to the details of the crystal potential and depend on such factors as the assumed atomic (or ionic) configuration, the method used to treat exchange and correlation, and self-consistency effects. For example, APW calculations for transition-metal oxides[39–41] involving neutral-atom potentials tend to overestimate the observed p-d gap by 1–3 eV.

One might expect similar errors in the present APW calculations for the transition-metal dichalcogenides since these results are based on the same neutral-atom model for the crystal potential. The present results for $1T$-HfS_2 provide a direct means for comparing the calculated and observed p-d gaps in these dichalcogenide layer compounds. The APW results for $1T$-HfS_2 in Fig. 3 yield a p-d indirect gap of 2.7 eV, which is 0.6-0.7 eV larger than the observed value.[12,13] If one attributes this error entirely to ionicity effects, then the present results suggest that the sulphides (and probably the selenides) are less ionic than the oxides. How-

ever, it is interesting to note that the Herman-Skillman[37] estimate of the Darwin and mass-velocity corrections for the atomic Hf $5d$ level is -0.05 Ry, or precisely the value that is required to bring the calculated and observed band gaps in $1T$-HfS_2 into complete agreement.

White and Lucovsky[48] present arguments based on the results of infrared reflectivity measurements that the octahedral group-IVB $1T$-TX_2 compounds are purely ionic whereas the trigonal-prismatic group-VIB $2H$-TX_2 compounds are covalent. The present APW results for these materials suggest no such clear cut change in either the bonding or ionicity in passing from the group-IVB to the

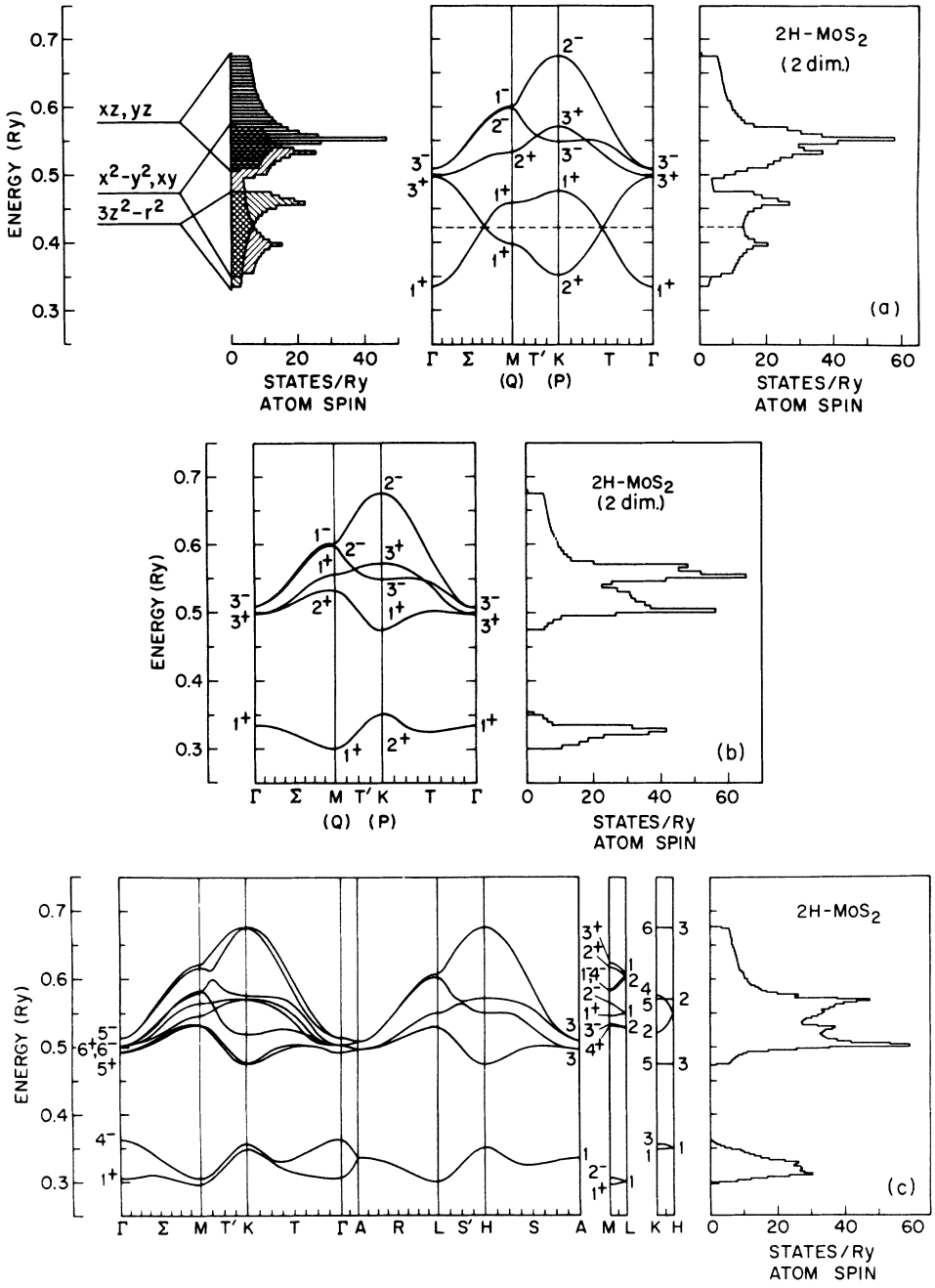

FIG. 11. (a) Ligand-field levels, LCAO $E(\vec{k})$, and density-of-states curves for $2H$-MoS_2 neglecting interband hybridization and interlayer interactions. (b) LCAO results for $2H$-MoS_2 with hybridization effects included. (c) LCAO results for $2H$-MoS_2 including interlayer interactions.

group-VI*B* compounds. The fact that the calculated *p-d* band separation decreases as one proceeds from the group-IV*B* to the group-VI*B* compounds certainly increases the extent of the covalent bonding as one moves to the right in the Periodic Table. However, it seems unlikely that the ionicity would decrease from +4 to 0 within this sequence of compounds. Based on the results of self-consistent calculations on somewhat analogous transition-metal compounds such as NbN[49] and the MnO_4^- cluster,[50] I would estimate that the effective metal-atom charge is never greater than about +1 in the dichalcogenides.

As a result of these difficulties and uncertainties, the present APW calculations are unable to provide a reliable prediction as to whether or not the metal *d* bands overlap the top of the chalcogen *p* bands in the group-V*B* and group-VI*B* compounds. HDHJ[9] were the first to suggest a model with overlapping *d* and *p* bands for these compounds. Originally, this was done to explain the fact that the transport measurements[23] on 2*H*-$NbSe_2$ and 2*H*-$TaSe_2$ samples indicate that the conductivity changes from *n* to *p* type as a function of tempera-

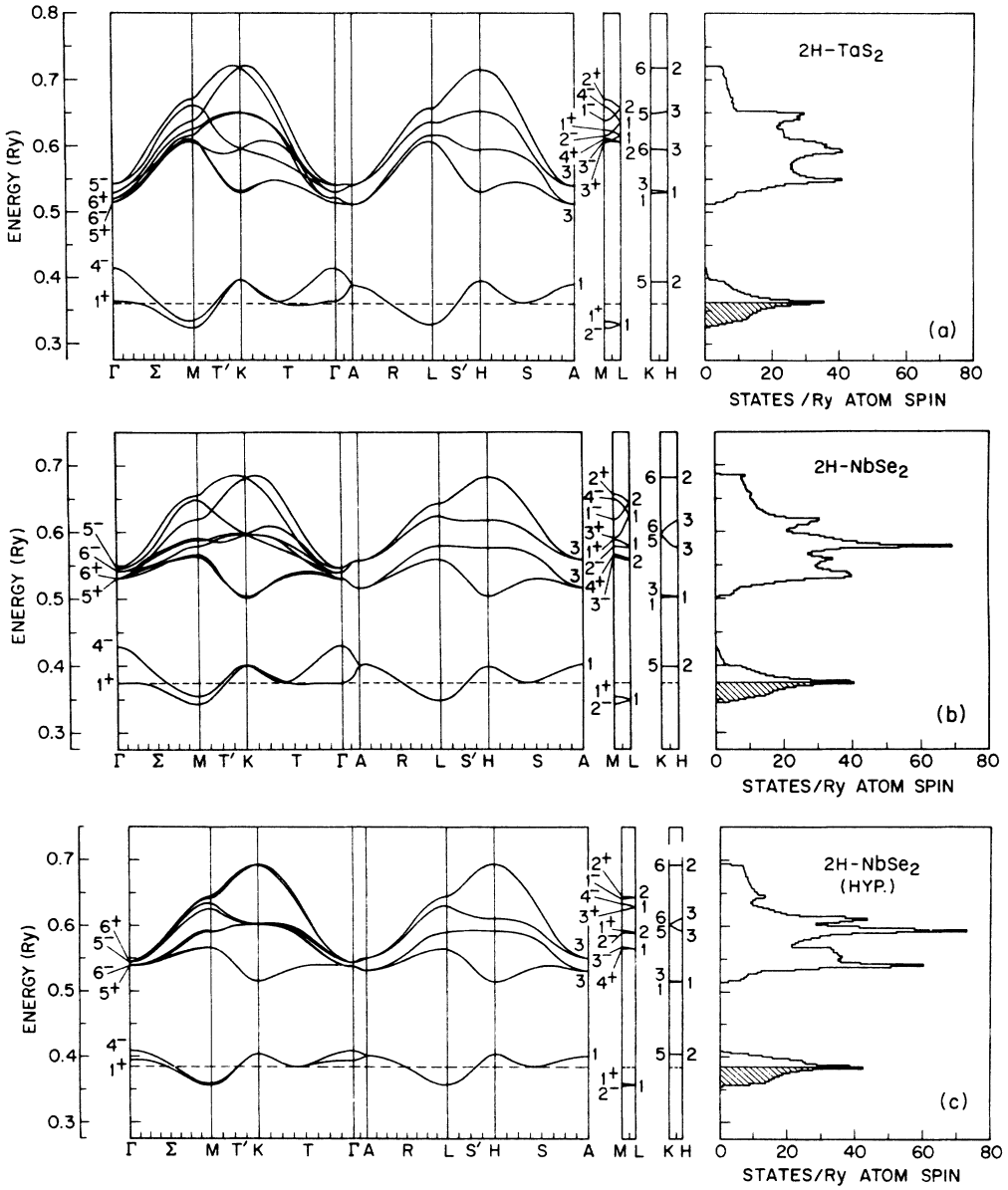

FIG. 12. LCAO results for (a) 2*H*-TaS_2; (b) 2*H*-$NbSe_2$; (c) hypothetical 2*H*-$NbSe_2$ with expanded interlayer separation.

ture. However, as Title and Shafer[32] point out this model is no longer necessary since the NMR[24] and x-ray[25] data show that this anomaly is associated with a structural transformation. In addition, Bromley[51] has shown that conduction via both holes and electrons can occur in $2H$-$NbSe_2$ if interlayer interactions are considered. The present APW-LCAO results predict that the $2H$-$NbSe_2$ Fermi surface contains only holelike carriers.

There are several aspects of Bromley's band-structure model for $2H$-$NbSe_2$ that deserve comment. In two dimensions, this model is simply the d_{z^2} band shown in Fig. 11(a) connecting the states with Γ_1^+, M_1^+, and K_1^+ symmetry. Unlike the results shown in this figure, Bromley assumes that this d_{z^2} band is split off in energy from the other d subbands. The present APW-LCAO results provide reliable estimates of Bromley's tight-binding parameters D and δ. These parameters represent the effective d-d interactions between nearest-neighbor d_{z^2} orbitals within a single layer and in adjacent layers, respectively. The LCAO results shown in Fig. 12(b) correspond to $D = 0.0114$ Ry and $\delta = 0.0044$ Ry, or $\delta/D = 0.39$. As discussed in Sec. V, second-neighbor interlayer effective interactions are significant in $2H$-$NbSe_2$ for the d_{z^2}-type orbitals. It is found that these second-neighbor interlayer parameters are about $\frac{1}{3}$ the magnitude of δ. However, their effect on the band structure is enhanced by the fact that there are six times as many of these second neighbors as there are nearest neighbors in $2H$-$NbSe_2$.

The present APW results for $2H$-$NbSe_2$ predict a Fermi surface that includes four separate hole-like sheets. In the first zone, these include a closed hole-type surface centered about the point A in Fig. 2 and an open cylindrical surface along the KH line. The closed surface extends close to but fails to contact the ΓMK plane if Γ_1^+ lies below the Fermi level, as shown in Fig. 6. Otherwise, this sheet would also be open along the c axis. The second zone contains two open cylindrical hole surfaces that are centered about the ΓA and KH lines, respectively, and enclose the first-zone sheets. These first- and second-zone sheets are degenerate in the ALH plane is spin-orbit coupling is neglected. According to Fig. 5, a similar Fermi surface is predicted for $2H$-TaS_2, though in this case, all the sheets are open.

Graebner[52] has observed magnetothermal oscillations in $2H$-$NbSe_2$. The angular dependence of the data suggests that it arises from orbits on a closed pancake-shaped Fermi-surface sheet whose diameter is at least five times its thickness. Neither the present APW-LCAO results nor Bromley's tight-binding model provides a reasonable explanation for these data. It seems likely that one must consider the effects of the 40 °K phase transition[23-25] on the $2H$-$NbSe_2$ band structure in order to interpret these Fermi-surface results. This represents a serious complication since, according to Marezio *et al.*,[25] the size of the $2H$-$NbSe_2$ unit cell is quadrupled at temperatures below the 40 °K phase transition. When the undistorted energy bands shown in Fig. 6 are folded into the reduced low-temperature Brillouin zone, the number of conduction bands increases from two in the high-temperature phase to eight in the distorted phase. As a result, one expects significant changes in both the Fermi-surface dimensions and topology in $2H$-$NbSe_2$ at low temperatures.

The most direct empirical information concerning the relative positions of metal d and chalcogen p bands in the group-VB and group-VIB TX_2 compounds is obtained from optical and photoemission data. We consider first the optical properties and attempt to understand the gross features of the low-energy data in terms of a joint-density-of-states (JDS) model for direct transitions within the d manifold, assuming constant interband matrix elements.

The JDS curve for direct d-d transitions in $2H$-MoS_2 is shown in Fig. 13. These results are derived from the LCAO band structure of Fig. 11(c). The energies at which structure is observed in the transmission spectrum are labeled, using the notation of Wilson and Yoffe[1] and Beal *et al.*[31] The vertical arrow indicates the energy at which transitions from the sulfur $3p$ to the unoccupied molyb-

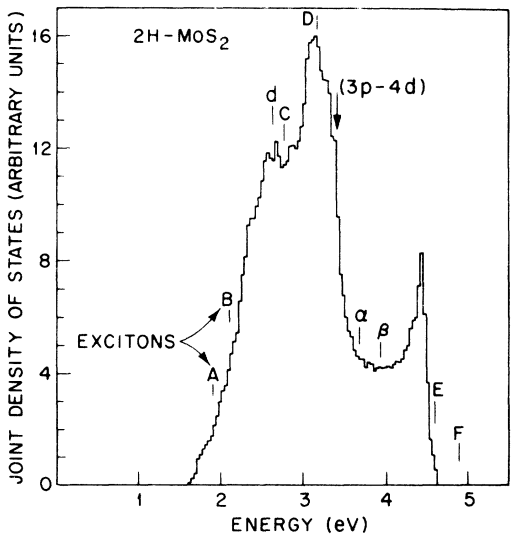

FIG. 13. Joint-density-of-states curve for direct transitions within the $2H$-MoS_2 d manifold. The arrow indicates the energy at which sulfur $3p$-molybdenum $4d$ transitions commence, according to the results of Fig. 8.

denum 4*d* bands are expected to commence, according to the APW results of Fig. 8.

A comparison of this JDS curve with the 2*H*-MoS_2 transmission spectrum [(Figs. 22(a) and 1 of Refs. 1 and 31, respectively] suggests that the main absorption peak that is centered at 3 eV is due to *d*-*d* transitions. This differs from previous interpretations,[1,5,31] which attribute this structure to *p*-*d* transitions. It is interesting to note that Zeppenfeld's[53] ϵ_2 curve (imaginary part of the dielectric constant) for 2*H*-MoS_2 exhibits peaks at 3.0 and 4.5 eV, which is in good agreement with the JDS curve shown in Fig. 13. We conclude that there is no direct evidence in the 2*H*-MoS_2 optical data for the occurrence of *p*-*d* transitions at energies below 3–4 eV. This suggests that the *A* and *B* excitons that are observed[1,31] at energies of 1.9 and 2.1 eV, respectively, in 2*H*-MoS_2 involve *d*-*d*[8,9] rather than *p*-*d* transitions.[1,5,31]

The results of similar JDS calculations for the group-V*B* 2*H*-TX_2 compounds are shown in Fig. 14. Though there are no optical data available for 2*H*-TaS_2, Wilson and Yoffe[1] compare the transmission spectra of 2*H*-$NbSe_2$ and 2*H*-TaS_2. These data exhibit prominent absorption peaks that begin at energies of 2.0 and 2.3 eV and rise to well-defined maxima at 2.8 and 3.2 eV, respectively. This behavior is in qualitative agreement with the JDS results for 2*H*-$NbSe_2$ and 2*H*-TaS_2 which are shown in Figs. 14(b) and 14(a), respectively.

We note in Fig. 14 that a 1.5–2.0-eV window occurs in the JDS curves for 2*H*-$NbSe_2$ and 2*H*-TaS_2 between 0.5 and 2.3 eV. According to the optical data, the absorption is small but finite within this energy range. We attribute this absorption to *p*-*d* transitions from the filled chalcogen *p*-type valence bands to the empty metal *d* bands just above the Fermi level, in agreement with the interpretation of Wilson and Yoffe.[1] Although these transitions are omitted from the JDS curves of Fig. 14, we indicate the threshold energies where these transitions are expected to commence, using the energy-band results of Figs. 5 and 6. From the fact that the optical absorption remains finite throughout this energy range, we infer that the *p*-*d* band separation is very nearly zero in both 2*H*-TaS_2 and 2*H*-$NbSe_2$.

This is consistent with the results of ultraviolet photoemission (PE) studies on these compounds.[18,30,54–56] These data suggest that the *p*-*d* band overlap is about 0.1–0.2 eV in both 2*H*-$NbSe_2$ and 2*H*-MoS_2. The PE data also resolve the controversy[1,9] regarding the magnitude of the semiconducting gap in the group-VI*B* compounds. These results demonstrate that this gap is at least 1 eV in 2*H*-MoS_2[18,30,55] and 2*H*-$MoTe_2$,[18,56] which is consistent with the present APW results for 2*H*-MoS_2. These PE data[18] also provide estimates of the occupied 4*d* bandwidths in 2*H*-$NbSe_2$ that agree well with the present calculated results.[10] Similar agreement is obtained for the chalcogen *p* bandwidths.

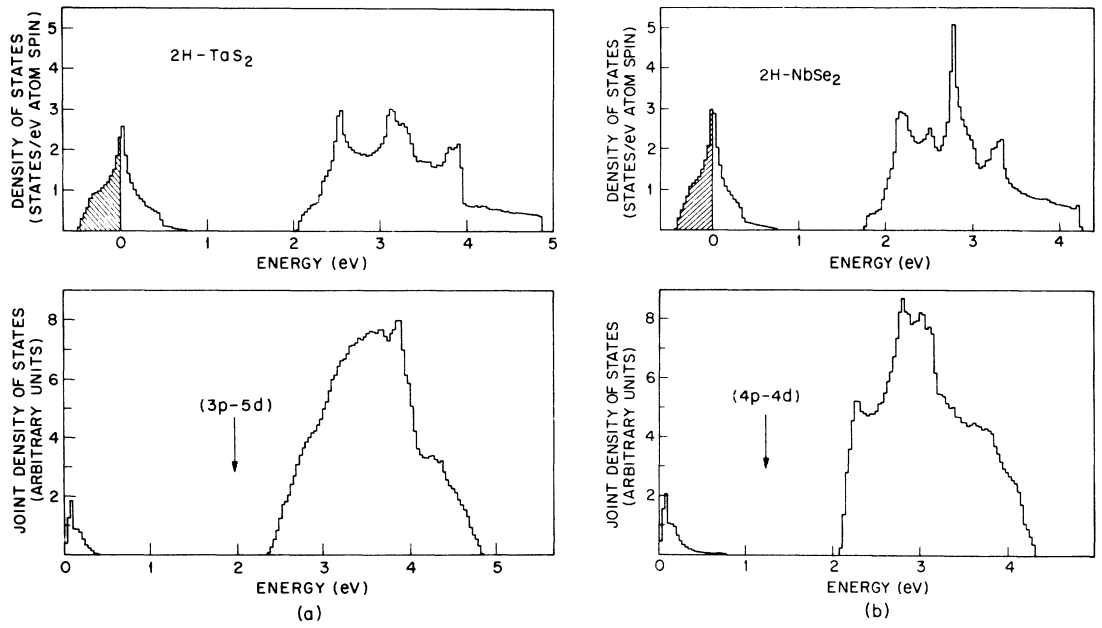

FIG. 14. Density-of-states and joint-density-of-states results for (a) 2*H*-TaS_2 and (b) 2*H*-$NbSe_2$. The vertical arrows indicate the threshold energies where *p*-*d* transitions are expected to commence.

If the p-d band separation in Figs. 4–8 is reduced until these bands overlap by 0.1–0.2 eV, then the top of the p valence band will be close to but below the Fermi level in the group-VB 2H-TX_2 compounds. In 2H-MoS_2, where the valence bandwidth is about 1 eV, a 0.1–0.2-eV overlap would leave the valence-band maximum at Γ, where the orbitals have d_{z^2} type symmetry. This result is consistent with the results of electron paramagnetic resonance studies on doped 2H-MoS_2 samples by Title and Shafer.[32] It provides additional support for interpreting the 1.9- and 2.1-eV excitons in 2H-MoS_2 in terms of d-d transitions.

In the case of the metallic group-VB 2H-TX_2 compounds, we can compare the experimental and theoretical values for the band density of states at the Fermi energy, $N(E_F)$. In the case of 2H-$NbSe_2$, the agreement is quite good. The empirical value of 2.8 states/eV spin Nb atom is derived from heat-capacity[26] and superconductivity[27] data, using McMillan's formula.[57] This agrees well with the value of 3.0 states/eV spin Nb atom that is shown in Fig. 14(b) for 2H-$NbSe_2$. This implies that the low-temperature phase transition[24,25] in 2H-$NbSe_2$ has a small effect on the density of states at the Fermi level. This is consistent with the fact that the magnetic susceptibility is essentially unchanged as the temperature is lowered through the 40 °K phase transition.[25]

On the other hand, the susceptibility data for 2H-TaS_2 exhibits a sharp decrease just below the 70 °K phase transition.[16,22] The simplest interpretation of this result involves a structural transformation that reduces the band density of states at the Fermi level. According to the heat-capcity data,[21] the phonon-enhanced density of states is 1.8 states/eV spin Ta atom, which is smaller than the calculated band density of states $N(E_F) = 2.3$ states/eV spin Ta atom. The effects of phonon enhancement of the thermal density of states will only increase this discrepancy.

The present APW-LCAO calculations for the group-VB 2H-TX_2 compounds suggest that the lattice instabilities that have been observed in these compounds may be caused by the very sharp peak in the density of states at the Fermi energy, as shown in Figs. 12 and 14. As Labbé and Friedel[58] have shown, the existence of fine structure in the density of states near the Fermi energy can lead to a Jahn-Teller-type distortion which splits this density-of-states peak and thereby reduces the free energy of the system at low temperatures.

Ehrenfreund *et al.*[24] estimate that the upper limit to the possible charge redistribution between the two niobium sites in 2H-$NbSe_2$ below 40 °K is about 0.1 electron. This suggests a splitting of the density-of-states peak $\delta E = \Delta n/N(E_F) = 0.03$ eV, which is comparable with the calculated 0.07-eV peak width. If this splitting were somewhat larger in 2H-TaS_2, then one would expect a lower minimum between the occupied and unoccupied peaks, and this could explain the relatively small value for $N(E_F)$ that is derived from the low-temperature heat-capacity data for this compound. This model suggests that $N(E_F)$ (and probably the superconducting transition temperature) should increase if one could suppress the 70 °K phase transition in 2H-TaS_2 by quenching or some other means.

The present APW-LCAO results for 1T-TaS_2 provide little insight into the nature of the metal-semiconductor transition that is observed at 350 °K. The calculated conduction bandwidth of 4 eV suggests that this transition is caused by a lattice distortion rather than a Mott transition. A complete determination of the low-temperature crystal structure for 1T-TaS_2 would be required before one could speculate further on this matter. Recent electron-diffraction studies[19] suggest that the room-temperature phase is very complex. Superlattice patterns indicate that 1T-TaS_2 is pseudohexagonal at room temperature, with $a' \approx 37\sqrt{13}\,a$.

Finally, HDHJ[9] have applied a ligand-field model to determine the relative stability of the trigonal-prismatic and octahedral TX_6 complexes for systems with d^0, d^1, and d^2 configurations. In this calculation, they assume that the electron-interaction terms are identical for both geometries so that the difference in total energies is proportional to the difference in the sums of the one-electron energies for each system. The present results show that band-structure effects represent an important factor in the stabilization process, particularly the 1-eV hybridization gap that occurs in the conduction band of the 2H phase.

We can show that this hybridization gap is relatively unimportant in the case of the group-VB compounds. From the present APW-LCAO results for 1T-TaS_2 and 2H-TaS_2, we find that the Fermi energies for these phases agree to within 0.2 eV. Relative to the vacuum, the average band energies per d electron in 1T-TaS_2 and 2H-TaS_2 are -0.60 and -0.59 Ry, respectively. The similarity in these values is consistent with the fact that both polytypes are metastable at low temperatures.

In the group-VIB compounds, the hybridization gap lowers substantially the average d-band energy for the 2H-TX_2 compounds relative to that for the 1T phase. This probably accounts for the fact that the group-VIB compounds never form with the 1T phase. This argument can also be extended to more complicated polytypes. For example, we note that the group-VIB compounds form only the 2H and 3R polytypes where the coordination is trigonal prismatic whereas the group-VB compounds include structures where the coordination is octa-

hedral (1*T*), trigonal prismatic (2*H*, 3*R*, 4*Ha*), or a combination of the two (4*Hb*, 6*R*).

Note added in manuscript. Kasowski[59] has recently published energy-band results for 2*H*-MoS_2 and 2*H*-NbS_2. These were calculated using the simplified linear-combination-of-muffin-tin-orbitals (LCMTO) method.[60] Although both the present APW and Kasowski's LCMTO calculations involve crystal potentials that should in principle be identical, the energy-band results are in fact quite different. The most significant difference concerns the width of the valence and conduction bands in 2*H*-MoS_2 and 2*H*-NbS_2. Kasowski finds that these bandwidths are about 2.7 and 3.1 eV, respectively. These values are about $2\frac{1}{2}$ times larger than those obtained in the present APW calculation for 2*H*-MoS_2 and 2*H*-$NbSe_2$. He attributes these differences to the "non-muffin-tin part of the potential."

I believe that this explanation for these discrepancies is incorrect. As discussed in Sec. III, the present APW calculations include the corrections to the muffin-tin potential in the region outside the APW spheres exactly.[39] Thus, the only remaining simplifying assumption in the APW potential involves the nonspherical terms within the APW spheres. By means of a calculation that will be discussed shortly, I find that these nonspherical corrections in 2*H*-$NbSe_2$ are about 10 times smaller than the 1.8–2.0-eV discrepancy between the calculated LCMTO and APW bandwidths. In fact, it is found that these nonspherical corrections further reduce the APW bandwidth in 2*H*-$NbSe_2$ by 0.18 eV, thereby enhancing this discrepancy. Therefore, I believe that the origin of this discrepancy lies in the LCMTO calculation.

There is a second feature in Kasowski's LCMTO results for 2*H*-NbS_2 that deserves comment. This concerns the changes in the conduction-band states when the potential in the region between the layers is set equal to zero. Although one would expect that this artificial potential barrier would reduce the strength of the effective *d*-*d* interlayer interactions, Kasowski's results imply that these interlayer interactions are actually enhanced in this situation. In particular, he finds that the conduction-band splittings at Γ $[E(\Gamma_4^-) - E(\Gamma_1^+)]$ and M $[E(M_2^-) - E(M_1^+)]$ increase rather than decrease when this zero-potential barrier is imposed between the layers. This is opposite to the trend shown in Figs. 6 and 7, where these splittings decrease as the interlayer separation (and consequently, the interlayer potential barrier) is increased.

In order to estimate the magnitude of the nonspherical corrections in these layer-type compounds, I have performed an additional APW calculation for 2*H*-$NbSe_2$ in which the niobium and selenium APW sphere radii of Table III were reduced by 15%. In the original calculation, the nonspherical terms of the potential just inside the niobium spheres varied from −0.45 to +0.20 Ry relative to the spherical average. The corresponding deviations within the selenium spheres were about $\frac{2}{3}$ as large. By shrinking these radii, one reduces the maximum nonspherical corrections just inside both spheres to the range −0.16 to +0.09 Ry. Of course, this increases the peak-to-peak variation of the nonconstant terms of the potential in the region outside the APW spheres (from 1.3 to 1.8 Ry), but this is not serious since these corrections are treated exactly in the APW method.

Relative to the results shown in Fig. 6, it is found that these nonspherical corrections shift the energies of the conduction-band states with Γ_1^+, Γ_4^-, M_1^+, and M_2^- symmetry by +0.004, −0.003, +0.007, and +0.010 Ry, respectively. Of course, there may be large percentage errors associated with these estimates since they involve energy differences which are comparable in magnitude to the estimated convergence of the APW eigenvalues in either calculation. With this in mind, let us summarize the over-all effect of these nonspherical corrections on the 2*H*-$NbSe_2$ band structure of Fig. 6. In general, it is found that these corrections lower the energies of states within the selenium 4*p* manifold by less than 0.02 Ry. One exception involves the valence-band state with Γ_2^- symmetry, where the shift is −0.04 Ry. This causes a slight increase in the 4*p*-4*d* energy separation and leaves Γ_2^- about 0.005 Ry above Γ_5^-. The corresponding corrections within the niobium 4*d* manifold tend to be positive and less than 0.01 Ry.

ACKNOWLEDGMENTS

I have enjoyed several beneficial discussions and conversations with my colleagues, particularly F. J. DiSalvo, T. H. Geballe, L. R. Testardi, and J. A. Wilson, on various aspects of this work. I am grateful to R. A. Bromley for pointing out some incorrect statements in the original manuscript regarding the 2*H*-$NbSe_2$ Fermi-surface topology.

[1]J. A. Wilson and A. D. Yoffe, Adv. Phys. **18**, 193 (1969).
[2]R. A. Bromley, Phys. Lett. **33A**, 242 (1970).
[3]R. A. Bromley and R. B. Murray, J. Phys. C **5**, 738 (1972).
[4]R. B. Murray, R. A. Bromley, and A. D. Yoffe, J. Phys. C **5**, 746 (1972).
[5]R. A. Bromley, R. B. Murray, and A. D. Yoffe, J. Phys. C **5**, 759 (1972).
[6]R. B. Murray and A. D. Yoffe, J. Phys. C **5**, 3038 (1972).

[7]D. R. Edmondson, Solid State Commun. **10,** 1085 (1972).
[8]J. B. Goodenough, Mater. Res. Bull. **3,** 409 (1968); Phys. Rev. **171,** 466 (1968).
[9]R. Huisman, R. DeJonge, C. Haas, and F. Jellinek, J. Solid State Chem. **3,** 56 (1971).
[10]L. F. Mattheiss, Phys. Rev. Lett. **30,** 784 (1973).
[11]J. C. Slater, *Quantum Theory of Molecules and Solids* (McGraw-Hill, New York, 1965), Vol. 2.
[12]L. E. Conroy and K. C. Park, Inorg. Chem. **7,** 459 (1968).
[13]D. L. Greenaway and R. Nitsche, J. Phys. Chem. Solids **26,** 1445 (1965).
[14]A. R. Beal, J. C. Knights, and W. Y. Liang, J. Phys. C **5,** 3531 (1972).
[15]A. H. Thompson, F. R. Gamble, and J. F. Revelli, Solid State Commun. **9,** 981 (1971).
[16]A. Menth, R. H. Geballe, and F. R. Gamble, Bull. Am. Phys. Soc. **16,** 403 (1971); F. J. DiSalvo, B. G. Bagley, J. M. Voorhoeve, and J. V. Waszczak, J. Phys. Chem. Solids **34,** 1357 (1973).
[17]L. E. Conroy and K. R. Pisharody, J. Solid State Chem. **4,** 345 (1972).
[18]P. M. Williams and R. F. Shepherd, J. Phys. C **6,** L36 (1973).
[19]J. A. Wilson, F. J. DiSalvo, and S. Mahajan, Bull. Am. Phys. Soc. **18,** 386 (1973).
[20]M. H. Van Maaren and G. M. Schaeffer, Phys. Lett. **24A,** 645 (1967).
[21]F. J. DiSalvo, R. Schwall, T. H. Geballe, F. R. Gamble, and J. H. Osiecki, Phys. Rev. Lett. **27,** 310 (1971).
[22]A. H. Thompson, F. R. Gamble, and R. F. Koehler, Jr., Phys. Rev. B **5,** 2811 (1972).
[23]H. N. S. Lee, M. Garcia, H. McKinzie, and A. Wold, J. Solid State Chem. **1,** 190 (1970).
[24]E. Ehrenfreund, A. C. Gossard, F. R. Gamble, and T. H. Geballe, J. Appl. Phys. **42,** 1491 (1971).
[25]M. Marezio, P. D. Dernier, A. Menth, and G. W. Hull, Jr., J. Solid State Chem. **4,** 425 (1972).
[26]M. H. Van Maaren and H. B. Harland, Phys. Lett. **29A,** 571 (1969).
[27]R. Bachmann, H. C. Kirsch, and T. H. Geballe, Solid State Commun. **9,** 57 (1971).
[28]W. Y. Liang, J. Phys. C **6,** 551 (1973).
[29]R. Dickinson and L. Pauling, J. Am. Chem. Soc. **45,** 1466 (1923).
[30]J. C. McMenamin and W. E. Spicer, Phys. Rev. Lett. **29,** 1501 (1972).
[31]A. R. Beal, J. C. Knights, and W. Y. Liang, J. Phys. C **5,** 3540 (1972).
[32]R. S. Title and M. W. Shafer, Phys. Rev. Lett. **28,** 808 (1972); Bull. Am. Phys. Soc. **18,** 47 (1973).
[33]R. Somoano, V. Hadek, and A. Rembaum, in *Superconductivity in d- and f-Band Metals*, edited by D. H. Douglas (American Institute of Physics, New York, 1972).
[34]L. F. Mattheiss, Phys. Rev. **151,** 450 (1966).
[35]L. F. Mattheiss, J. H. Wood, and A. C. Switendick, in *Methods in Computational Physics*, edited by B. Alder, S. Fernbach, and M. Rotenberg (Academic, New York, 1968).
[36]J. C. Phillips, Phys. Rev. Lett. **28,** 1196 (1972).
[37]F. Herman and S. Skillman, *Atomic Structure Calculations* (Prentice-Hall, Englewood Cliffs, N. J., 1963).
[38]J. C. Slater, Phys. Rev. **81,** 385 (1951).
[39]L. F. Mattheiss, Phys. Rev. **181,** 987 (1969).
[40]L. F. Mattheiss, Phys. Rev. B **5,** 290 (1972); Phys. Rev. B **5,** 306 (1972).
[41]L. F. Mattheiss, Phys. Rev. B **6,** 4718 (1972).
[42]C. Herring, J. Franklin Inst. **233,** 525 (1942).
[43]C. Y. Fong and M. L. Cohen, Phys. Rev. B **5,** 3095 (1972).
[44]L. F. Mattheiss, Phys. Rev. B **2,** 3918 (1970).
[45]J. C. Slater and G. F. Koster, Phys. Rev. **94,** 1498 (1954).
[46]R. F. Egorov, B. I. Reser, and V. P. Shirokovskii, Phys. Status Solidi **26,** 391 (1968).
[47]M. Miasek, Phys. Rev. **107,** 92 (1957).
[48]R. M. White and G. Lucovsky, Solid State Commun. **11,** 1369 (1972).
[49]K. Schwarz, Monatsh. Chem. **102,** 1400 (1971).
[50]K. H. Johnson and F. C. Smith, Jr., Phys. Rev. B **5,** 831 (1972).
[51]R. A. Bromley, Phys. Rev. Lett. **29,** 357 (1972).
[52]J. E. Graebner, Bull. Am. Phys. Soc. **18,** 386 (1973).
[53]K. Zeppenfeld, Opt. Commun. **1,** 377 (1970).
[54]R. H. Williams and A. J. McEvoy, Phys. Status Solidi **47,** 217 (1971).
[55]R. H. Williams, J. M. Thomas, M. Barber, and N. Alford, Chem. Phys. Lett. **17,** 142 (1972).
[56]R. H. Williams, J. Phys. C **6,** L32 (1973).
[57]W. L. McMillan, Phys. Rev. **167,** 331 (1968).
[58]J. Labbé and J. Friedel, J. Phys. Radium **27,** 153 (1966); J. Phys. Radium 303 (1966).
[59]R. V. Kasowski, Phys. Rev. Lett. **30,** 1175 (1973).
[60]R. V. Kasowski and O. K. Andersen, Solid State Commun. **11,** 799 (1972).